


Statistical study of vacancy diffusion in TiC and TaC

Xiaochuan Tang,^{1,*} Rofiques Salehin,¹ Gregory B. Thompson,² and Christopher R. Weinberger^{1,3}¹Department of Mechanical Engineering, Colorado State University, Fort Collins, Colorado 80523, USA²The University of Alabama, Department of Metallurgical and Materials Engineering, 401, 7th Avenue, 285 Hardaway Hall, Tuscaloosa, Alabama 35487, USA³School of Advanced Materials Discovery, Colorado State University, Fort Collins, Colorado 80523, USA (Received 24 March 2020; revised 9 June 2020; accepted 19 August 2020; published 2 September 2020)

Density functional theory (DFT) simulations, Metropolis Monte Carlo (MMC), and kinetic Monte Carlo (kMC) simulations were performed to understand the mechanisms of mass diffusion in a group IVB transition metal carbide, TiC, and a group VB transition metal carbide, TaC. The DFT calculations were used to obtain the vacancy formation energy and migration energy of a variety of microstates for off-stoichiometric TiC and TaC. MMC simulations, based on our DFT results, were used to determine the ensemble average of the metal vacancy formation energy and determine the average size metal-vacancy clusters present in these materials. kMC simulations were used to determine the ensemble average of the migration energy barrier as well as understand how the vacancies in these materials, on average, migrate. These collective results show that metal vacancy migration in TiC and TaC are quite different, where Ti vacancies should be surrounded by four to five carbon vacancies whereas, on average, tantalum vacancies are surrounded by one or zero carbon vacancies. However, the carbon vacancies substantially contribute to metal vacancy diffusion in both these materials, as the metal vacancy statistically will have a carbon vacancy near it before and after migration. From these results, we find that the activation energy of metal vacancy diffusion is 7.66 eV in $\text{Ti}_{0.995}\text{C}_{0.97}$ and 6.41 eV in $\text{Ta}_{0.995}\text{C}_{0.97}$, which agrees reasonably well with experimentally reported activation energies. These results give further insights into the mechanisms associated with mass diffusion within the transition metal carbide families, an important insight needed to better elucidate high temperature diffusional creep responses which is often difficult to assess experimentally.

DOI: [10.1103/PhysRevMaterials.4.093602](https://doi.org/10.1103/PhysRevMaterials.4.093602)

I. INTRODUCTION

Transition metal carbides (TMCs) are one class of ultra-high-temperature ceramics (UHTCs), which are known for their high melting temperature, high hardness, and moderate oxidation resistance. In this class of materials, strong metal-metal bonds form between the transition metals as well as strong covalent bonds between the metal and carbon atoms which enhances the materials' structural and thermal stability at high temperatures [1]. The applications of TMCs are widespread and include wear resistant parts, thermal barrier coatings, cutting tools, and applications in nuclear energy [2]. However, when these materials experience significant loads at temperatures roughly above half their melting temperatures, they undergo classic creep deformation. Under an applied stress σ , the steady-state creep strain rate can be described by [3]:

$$\dot{\epsilon} = C\sigma^m \exp\left(-\frac{Q_c}{k_B T}\right), \quad (1)$$

where $\dot{\epsilon}$ is the creep strain rate, C is a material-dependent constant, m is the stress exponent, and Q_c is the activation energy for creep which is often equal to the activation energy for self-diffusion. Thus, understanding the activation energy

and diffusion mechanisms in the transition metal carbides is paramount in understanding their deformation mechanisms at extreme temperatures.

While there are a number of studies regarding the high temperature deformation of the TMCs, there are a limited number regarding the identification of their specific creep mechanisms. Chermant *et al.* [4] conducted three point bend tests on TiC in the range of 1673 ~ 2273 K and found the activation energy in the lower temperature range to be 5 eV, which was attributed to carbon (C) diffusion, and an activation energy of 7 eV in the upper temperature range, which was attributed to vacancy assisted mass (titanium) diffusion. Kim *et al.* [5] studied low temperature creep in $\text{TaC}_{0.99}$ between 1573 ~ 1973 K and reported the activation energy to be 4.3 eV, which was attributed to C diffusion too. Steinitz [6] conducted tensile tests of creep for $\text{TaC}_{0.92-0.99}$ above 2300 K and found an activation energy much higher, 7.2 ± 1.3 eV, which he attributed to tantalum (Ta) diffusion. Smith *et al.* [7] performed bending creep tests of $\text{TaC}_{0.98}$ between 2500 K to 2900 K and found an activation energy of 9.81 ± 1.6 eV. In that same report, using the same methodology, the authors found an activation energy of 7.1 ± 0.6 eV for the creep of $\text{HfC}_{0.98}$ between 2400 K and 2600 K. From these reports, creep in TMCs exhibit two temperature dependent deformation regimes: A high temperature regime presumably controlled by metal diffusion and a low temperature regime presumably controlled by C diffusion.

*Corresponding author: xtang@ucdavis.edu

As noted above, the deformation mechanisms in the group IVB and VB carbides are often attributed to either carbon (C) or metal (Me) atom diffusion, depending on the temperature range. The activation energies of C diffusion in these two groups are reported between 2 ~ 5 eV with a summary found in Ref. [8]. Here, we will specifically review the findings for TiC and TaC, the two compounds directly studied in this paper. For C diffusion in TiC, Sarian [9] used the isotope tracer method to measure the activation energy of $\text{TiC}_{0.97}$ and $\text{TiC}_{0.887}$ between 1723 ~ 2553 K and found activation energies of 4.094 ± 0.030 eV and 4.588 ± 0.026 eV, respectively. Eremeev *et al.* [10], using the same methods, measured the activation energy for C diffusion to be 1.152 ± 0.031 eV for $\text{TiC}_{0.4}$ between 2050 ~ 2380 K. van Loo *et al.* [11] expanded these carbon activation studies over a wide range of stoichiometries in TiC_{1-y} , where $y = 0.03 \sim 0.5$, using the diffusion-couple method. They noted that the diffusion coefficient depended on the vacancy concentration and reported an activation energy for C diffusion to be 3.115 ± 0.312 eV for temperatures between 1473 ~ 2023 K. For titanium (Ti) diffusion, Sarian [12] again used the isotope tracer method and reported an activation energy of 7.578 ± 0.155 eV for $\text{TiC}_{0.67-0.97}$ in the temperature range of 2193 ~ 2488 K.

The self-diffusion of C in TaC has primarily been studied by measuring the growth rates of the carbide layers to estimate the diffusivities of C in TaC and Ta_2C [13–15]. The reported values are therefore an average over TaC's composition range with reported activation energies of 3.9 eV [13], 3.7 eV [14], 4.3 eV [13], and 3.7 eV [15]. The authors are not aware of any measurements of Ta diffusion in TaC but do note that the activation energy for niobium (Nb) diffusion in NbC is 6.1 ± 0.1 eV [16]. While one should not assume the diffusion of Nb in NbC is the same as Ta in TaC, it does provide evidence that the activation energy for Me diffusion in the group VB carbides is substantially higher than that for C diffusion and similar to other high temperature activation energies for creep.

There have been more recent efforts made to obtain the activation energy for Me and C self-diffusion in TMCs from simulations. In these modeling approaches, the activation energy for self-diffusion is reported as the sum of the vacancy formation energy, E_{vf} , and the vacancy migration energy, E_{vm} , as determined from *ab initio* methods. Yu *et al.* [17] computed activation energies for C diffusion using density functional theory (DFT) [18] in all the group IVB and VB TMCs, reporting values of 4.1 eV in TiC and 4.3 eV in TaC. Råsander *et al.* [19] performed calculations of the C vacancy formation and migration energy in TiC and reported the activation energy for C diffusion to be about 4.3 eV. Razumovskiy *et al.* [20] computed the activation energy of Me diffusion for a single Me vacancy in TiC and ZrC and noted the activation energy for Ti self-diffusion was about 13 eV. The authors further pointed out that the activation energy for C diffusion agreed with experiments but that the activation energy for Me diffusion was quite high compared to prior experiment findings.

This disagreement with the experimentally measured activation energy for Ti diffusion in TiC has led to a few investigations into how Me atom diffusion might occur in these transition metal carbides. Notably, Razumovskiy *et al.* [21] have proposed a vacancy clustering mechanism whereby

the Ti atom vacancy is surrounded by a cluster of C vacancies that ranges from 1 to 6. They pointed out that the C vacancy cluster helps to substantially lower the vacancy formation energy of the Ti atom and, by adding the formation and migration energy, found that the lowest activation energy (6.83 eV) is associated with the Ti vacancy surrounded by 6 C vacancies. They conclude that this clustering mechanism is likely responsible for Me atom diffusion in TMCs. In contrast, Sun *et al.* [22] recently proposed a mechanism by which Ti interstitials surrounded by two C vacancies can also result in mass diffusion and has a combined activation energy of 7.28 eV. Because of the closer agreement of the activation energy with experiments, they concluded that this must be the mechanism.

While both of these studies propose new and important mechanisms, they each are limited to a small number of microstates and the activation energy associated with that microstate. Actual mass diffusion in TMCs should occur via random motion and is unlikely to be associated with a single microstate studied in DFT. It is unclear how important single microstates contribute to the experimentally measured activation energies. Furthermore, all of the studies to date have focused on TiC and thus are only applicable to the group IVB carbides, despite the claim that they are general [21]. It is well known that the group VB and IVB carbides actually have differences in bonding that results in differences in stacking faults energies and slip planes [23,24] as well as differences in the phases that they form [25,26]. Therefore, we do not expect that the metal atom diffusion processes in the two groups should be the same.

The purpose of the current work is to gain insight into vacancy mobility in two bulk transition metal carbides, TiC and TaC, from statistical studies on nearly stoichiometric TMCs ($\text{Me}_{1-x}\text{C}_{1-y}$). This report consists of two parts: DFT calculations and Monte Carlo (MC) simulations. In the first part of this work, we use DFT to compute a large number of microstates of various Me-*n*C vacancy clusters to determine the vacancy formation energy, E_{vf} , of these clusters. Additionally, DFT simulations are utilized to compute the energy barrier for vacancy migration. In the second part of the paper, we use Monte Carlo simulations with the Metropolis-Hasting algorithm [27,28] (MMC) to estimate the average vacancy formation energies and kinetic Monte Carlo [29] (kMC) simulations to determine the average vacancy migration barriers for experimentally relevant temperatures between 2000 K to 2800 K. The MMC simulations provide not only the average vacancy formation energies but also the distribution of the fraction of each type of vacancy cluster. Similarly, kMC not only provides average migration energy values but also insight into exactly how these clusters move in the solid. Collectively, these results demonstrate that TiC does indeed diffuse by a cluster mechanism with a Ti vacancy surrounded by four or five C vacancies, while TaC moves primarily as a bound divacancy.

II. METHODOLOGY

From the perspective of vacancy assisted atomic diffusion [30], diffusion requires both sufficient thermal energy such that a sufficient number of vacancies are present for mass

diffusion as well as to overcome the energy barrier, Δg_{vm} , for migration. In thermal equilibrium, atoms in a crystal vibrate and possibly move to their adjacent vacant sites at a frequency ν_0 in an attempt to overcome the diffusion migration energy barrier. The rate of overcoming the energy barrier and the probability of having a vacancy next to it both follow the Boltzmann distribution at constant temperature and thus traditionally we add the migration energy barrier, Δg_{vm} , to the vacancy formation energy, Δg_{vf} . Therefore, the self-diffusion coefficient via the vacancy mechanism is typically written as:

$$D = \frac{z\nu_0 d^2}{6} \exp\left(-\frac{\Delta g_{vf} + \Delta g_{vm}}{k_B T}\right), \quad (2)$$

where d is the jump distance, which is usually the nearest-neighbor distance, and z is the number of nearest-neighbor sites. From thermodynamics, we can write $\Delta g = \Delta h - T\Delta s$, which allows the diffusion coefficient to be rewritten as:

$$D = D_0 \exp\left(-\frac{Q_a}{k_B T}\right), \quad D_0 = \frac{z\nu_0 d^2}{6} \exp\left(\frac{\Delta s_{vf} + \Delta s_{vm}}{k_B}\right), \quad (3)$$

where $Q_a = \Delta h_{vf} + \Delta h_{vm}$ is the activation enthalpy for vacancy diffusion and D_0 is the diffusion coefficient pre-factor. Therefore, if we can obtain the ensemble average of the vacancy formation energy, $\langle E_{vf} \rangle$, and the vacancy migration energy, $\langle E_{vm} \rangle$, from atomic-level simulations, we can approximate the value of the activation enthalpy. Here, we develop several models based on energies and jump frequencies obtained from DFT calculations to carry out our MMC and kMC simulations, all of which will be described below.

A. DFT calculations of formation energies

In order to calculate the total energies of the defected microstates, we performed DFT calculations using a plane wave basis and projected-augmented-wave (PAW) [31,32] pseudopotentials as implemented in the Vienna *ab initio* simulation package (VASP). The exchange correlation energies were computed via the generalized gradient approximation (GGA) [33] using the formulation of Perdew-Burke-Ernzerhof (PBE) [34]. The cutoff energy and energy convergence criteria were chosen to be 450 eV and 10^{-5} eV, respectively. The k -point density was chosen to be $12 \times 12 \times 12$ for the eight-atom conventional unit cell of the B1 structure, the standard structure of TiC and TaC.

In order to assure our DFT simulation cells were sufficiently large, we studied the defect formation energies, to be defined below, as a function of the number of atoms in the supercell. The supercells in our simulation were generated as the repetition of both a conventional cell and a primitive cell along three lattice vectors uniformly. An arbitrary Me atom was removed in each of those supercells resulting in our supercells containing 15, 31, 53, 63, 127, 215, and 249 atoms, respectively. The convergence test was based on the energy difference between the single-point-defect structure and its corresponding pure structure. These results show that the energy difference converges within 0.1 eV for supercells with 63 atoms or more. Therefore, for consistency in our simulations and to allow for a margin of error, we selected the supercell with 128 atoms generated from the $4 \times 4 \times 4$

repetition of a primitive cell and a k -point integration scheme of $5 \times 5 \times 5$ to conduct all of our simulations.

The vacancy formation energy, E_{vf} , is the increase in energy of the system when an atom is removed from a lattice site an placed into and equivalent site elsewhere in the crystal. We can approximate the isolated vacancy formation energy, E_{vf}^{iso} , in DFT, as:

$$E_{vf}^{\text{iso}}(\text{Me}) = E[N - 1, 1, 0] + \mu(\text{Me}) - E[N, 0, 0], \quad (4)$$

$$E_{vf}^{\text{iso}}(\text{C}) = E[N - 1, 0, 1] + \mu(\text{C}) - E[N, 0, 0], \quad (5)$$

where E represents the total energy of a microstate and μ stands for the chemical potential. In this work, the nomenclature $E[N - m - n, m, n]$ is used where N represents the number of atoms in the pure structure, m is the number of Me vacancies and n is the number of C vacancies. It is noteworthy to mention that the ground-state energy computed in VASP has an arbitrary zero-energy reference. To ensure that the values reported in this paper have a physical meaning, we subtract off the energies of the appropriate number of isolated atoms (Me and C) from the VASP calculations. Thus, the energies reported here are relative to all of the atoms separated infinitely far apart and, for a perfect system, represent the negative of the cohesive energy of the solid. The chemical potential of metal (Me) and carbon (C) atoms are defined as the derivative of the total energy for a system with respect to the molar fraction of the component, which is difficult to compute exactly in DFT. In this study, the chemical potentials were computed from the linear regression on the total energy for stoichiometric MeC, graphite, and the nearest stable metal-rich carbide found in DFT [17] (i.e., Ti_7C_6 and Ta_6C_5 , respectively). The regression was done to ensure the chemical potentials summed to the cohesive energy of the stoichiometric MeC compound following what we have done in previous studies [35,36]. The isolated vacancy formation energies obtained in our calculations are close to previously reported values [17,19,20] and are listed in Table V.

While the formation energy of a single defect is straightforward to calculate and use in the aforementioned diffusion equations, it is less clear how this should be handled for vacancy clusters. Different methods in previous works [19–21] have been introduced based on different interpretations. In this work, we consider two different methods to approximate the formation energy of a Me vacancy within a Me- n C vacancy cluster which we will describe below. First, consider a microstate with m Me vacancies and n C vacancies as illustrated in the middle frame of Fig. 1. The formation energy of this microstate can be computed relative to a reference state where vacancies are infinitely far away from each other, which means the interaction between those vacancies is zero. The energy of this reference state, which includes m Me and n C vacancies, denoted as $E_\infty[N - m - n, m, n]$, is:

$$E_\infty[N - m - n, m, n] = mE[N - 1, 1, 0] + nE[N - 1, 0, 1] - (m + n - 1)E[N, 0, 0]. \quad (6)$$

Now, if we remove a single Me vacancy, from this newly bound state as shown in Fig. 1 and compute the total energy as $E[N - m - n - 1, m + 1, n]$, we can write the formation

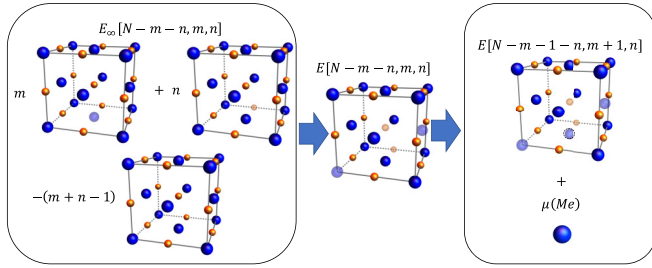


FIG. 1. The microscopic view for the Me vacancy formation inside the microstate with m Me vacancies and n C vacancies: solid blue and orange spheres stand for Me and C atoms, respectively, while transparent blue and orange stand for Me and C vacancies, respectively. The left frame illustrates the microstate with all isolated m Me vacancies and n C vacancies. The middle frame represents the microstate with a specific vacancies arrangement. The right frame illustrates the formation of a Me vacancy from the microstate in the middle frame.

energy of this defect in the cluster as:

$$E_{vf}^I(\text{Me}|m, n) = E[N - m - n - 1, m + 1, n] + \mu(\text{Me}) - E_{\infty}[N - m - n, m, n]. \quad (7)$$

This is similar to the method introduced in Ref. [21] but in our case we have a well defined reference state (infinitely separated vacancies). Thus, we can create a well defined interpretation of this formation energy—it represents the probability of finding the Me vacancy surrounded by other Me and C vacancies relative to the structure with the same number of noninteracting Me and C vacancies. However, these formation energies are not useful in Monte Carlo simulations. In each Monte Carlo step, the positions of atoms will be swapped and we must have formation energies that are directly related to the current configuration of the vacancies, not relative to infinitely separated vacancies. Thus, we define a second formation energy that is useful in MMC simulations as:

$$E_{vf}^II(\text{Me}|m, n) = E[N - m - n - 1, m + 1, n] + \mu(\text{Me}) - E[N - m - n, m, n]. \quad (8)$$

This is simply the difference between the atomic configurations with and without a Me vacancy. In a similar way, the vacancy formation energy of C in a cluster can be defined.

B. Models for the vacancy formation energy

To further investigate the vacancy-cluster formation in TiC and TaC, the ensemble average of the Me vacancy formation energy $\langle E_{vf}(\text{Me}) \rangle$ needs to be evaluated in MC simulations. In order to obtain $\langle E_{vf}(\text{Me}) \rangle$, we need a model for the Me vacancy formation energy that includes the arrangement of other existing vacancies. Thus, we developed a simple model, which we named the nearest-neighbor model (NNM), to represent the formation energies of simple vacancy clusters in hopes that such a model is sufficient for ensemble averaging. In the NNM, the Me vacancy formation energy depends on the number of C vacancies (n) in its nearest neighbor shell. The values of $E_{vf}^II(\text{Me})$ are computed from Eq. (8) using the definition II because the NNM is employed in MC simulations. For those Me- n C vacancy clusters that have more than one configuration

TABLE I. The metal (Me) vacancy formation energy as predicted by our nearest-neighbor model (NNM) computed using both definition I and II. When $n = 2, 3, 4$, we used the the average value of E_{vf} over all possible configurations. (All units are in eV.)

n C	0	1	2	3	4	5	6
$E_{vf}^I(\text{Ti})$	7.44	5.99	5.03	4.16	3.51	3.02	2.76
$E_{vf}^{II}(\text{Ti})$	7.44	5.99	4.72	3.74	2.35	1.03	0.05
$E_{vf}^I(\text{Ta})$	2.58	2.42	2.43	2.48	2.54	2.63	2.71
$E_{vf}^{II}(\text{Ta})$	2.58	2.42	2.26	2.00	1.57	0.95	0.20

($n = 2, 3, 4$), the value used in the NNM is the average value of $E_{vf}(\text{Me})$ over all possible configurations. Table I lists all the values of $E_{vf}^I(\text{Me})$ and $E_{vf}^{II}(\text{Me})$ in the NNM for both TiC and TaC.

The NNM may be very useful in determining the average formation energy due to its simplicity, however it clearly neglects interactions that could be important. To determine if these neglected interactions are important, we also developed a more complete model of the interaction energies of complex C and Me vacancies configurations. The model we used is a simple cluster expansion model (CEM) [37,38]. The CEM is a common method to approximate the total energy of a crystal in computational materials science [39,40]. However, instead of developing the expansion around atoms, we built it upon the configuration of vacancies. Furthermore, since it is easy to write the energy of a set of vacancies that are isolated, we built our cluster expansion around the vacancy binding energy of a cluster of vacancies.

To this end, we introduce the total vacancy binding energy, E_{vb} , which is the energy increase associated with bringing all of the vacancies from infinitely far away and binding them into the current configuration. Using our notation, we can then define this total vacancy binding energy as:

$$E_{vb} = E[N - m - n, m, n] - E_{\infty}[N - m - n, m, n]. \quad (9)$$

A negative E_{vb} indicates that forming the cluster of bound vacancies is energetically favorable. For example, the binding energy between a Me and C vacancy can be computed by setting $m = 1$ and $n = 1$, which we find directly from our DFT calculations to be -1.45 eV in TiC and -0.16 eV in TaC for the first shell Me-C vacancy pair, noted as $E_{vb}[(\text{Me-C})_{1st}]$. The negative values of $E_{vb}[(\text{Me-C})_{1st}]$ do suggest a tendency for vacancy aggregation of Me and C vacancies, however it is important to note that the vacancy binding energy is indeed microstate (configuration) dependent and we need a general model that can account for all possible configurations.

In this work, the CEM is based on ideal vacancy positions in the B1 structure for off-stoichiometric TiC and TaC. The total interactions of the vacancies in a microstate described by the CEM can be expressed as the combination of pairwise interactions and many-body interactions, where many-body interactions are corrections to the pairwise interactions. For simplicity, we neglected most of the higher-order corrections and only kept pairwise and three-body interactions. Since the vacancy interaction energies decay relatively quickly, we utilized a cutoff distance for both pairwise and three-body interactions of $\sqrt{10}a/2$ to render all interactions finite.

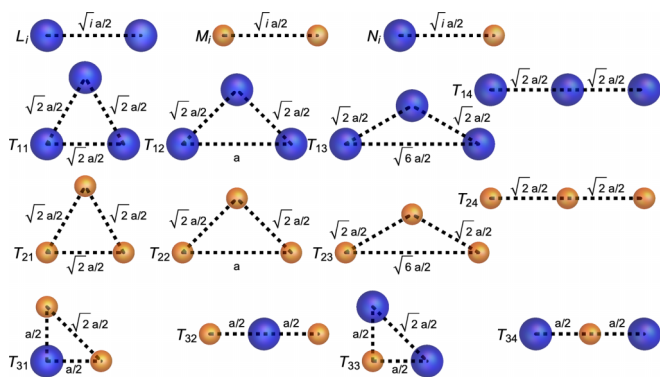


FIG. 2. In this work we used a cluster expansion to represent the energy of the different microstates including both pairwise and three body interactions as illustrated above. We illustrate some of the pairwise interactions and all of the three body interactions used in our cluster expansion. The blue and orange spheres represent Me and C vacancies, respectively.

In the MeC B1 structure, there are three types of vacancy pairs: Me-Me, C-C, and Me-C, which we denote as L_i , M_i , and N_j , respectively, in our cluster expansion, as shown in Fig. 2. The subscript i represents the vacancy pair with the intervacancy distance $\sqrt{ia}/2$, where a is the lattice constant in a conventional B1 unit cell. However, this means that, due to the B1 structure, not all the indices are used. For L_i and M_i , i is an even number from 2 to 10. However, for N_j , j must be odd (i.e., $j = 1, 3, 5, 9$). For the three-body interactions, we chose to model vacancy configurations which consist of a center vacancy and other two vacancies in its 1st shell, which we denote T_{ij} . The first index symbolizes the four categories of three-body interactions, Me-Me-Me, C-C-C, C-Me-C, and Me-C-Me, while the second subscript represents the possible spatial configurations. The first index ranges from 1 to 3 while the second index ranges from 1 to 4 and the configurations are illustrated in Fig. 2. Using the CEM, the total vacancy binding energy E_{vb} in a microstate is approximately:

$$E_{vb} = \varepsilon_0 + \sum_i \alpha_i L_i + \sum_i \beta_i M_i + \sum_j \gamma_j N_j + \sum_{l=1}^3 \sum_{k=1}^4 \delta_{lk} T_{lk}, \quad (10)$$

where Greek letters α , β , γ , and δ represent the energy associated to their corresponding vacancy configurations and the parameter ε_0 represents the total value of neglected higher-order corrections.

The parameters in Eq. (10) can then be determined using a standard fitting procedure to DFT data. We first calculated the energy of 110 microstates with random vacancy concentrations and positions via DFT. Then, in each microstate simulated in DFT, the vacancy binding energy E_{vb} was computed from Eq. (9). The best fit values of the constants were then determined using a least-square fitting [41] procedure to match the CEM predictions and DFT data. From the regression results, we computed the fitting residuals, the probability value [42] (p value) of each parameter, the coefficient of determination [43] (R^2), and the adjusted coefficient of determination [44] (\bar{R}^2). The probability value indicates the validity of the prediction from a regression model. From the

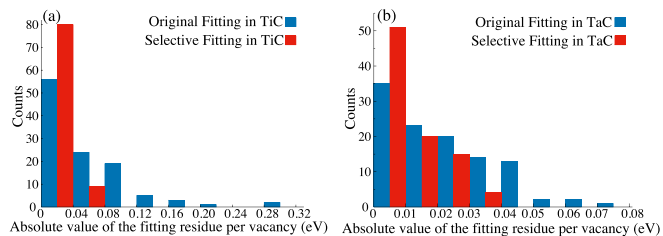


FIG. 3. A histogram of the fitting residues (in eV) per vacancy: (a) based on the energy of the microstates in TiC; (b) based on the energy of the microstates in TaC. The blue bars represent the fitting residues per vacancy from the least square fitting on all original 110 microstates and the red bars represent the fitting residues per vacancy from the least square fitting of selected microstates. In the original fittings, $R^2(TiC) = 0.957$, $\bar{R}^2(TiC) = 0.944$, $R^2(TaC) = 0.951$, and $\bar{R}^2(TaC) = 0.935$. In the selective fittings, $R^2(TiC) = 0.998$, $\bar{R}^2(TiC) = 0.997$, $R^2(TaC) = 0.994$, and $\bar{R}^2(TaC) = 0.990$.

original fitting on all 110 microstates, a few microstates have large deviations, on a per-vacancy basis, from the regression model, which are shown in Fig. 3. For some microstates, the deviations in E_{vb} per vacancy are larger than the uncertainty in our DFT calculations (0.1 eV) which suggests a need to re-evaluate the data used in our regression. After analyzing our data, we found that the microstates with large deviations in energy between the regression model and DFT data contained large vacancy clusters consisting of more than three Me vacancies and several C vacancies. The existence of a large vacancy cluster, especially a large number of Me atoms, causes substantial local deformation so that both vacancies and atoms move too far out of their perfect lattice sites. These large displacements violate the CEM, which assumes ideal atomic positions and explains the large model error. Therefore, we chose to specifically exclude those microstates from our fitting procedure. To obtain good statistical values of pairwise and three-body vacancy interactions, we excluded microstates in TiC with the deviations per vacancy larger than 0.1 eV from the original fitting. Similarly, we excluded microstates in TaC with the deviation per vacancy larger than 0.05 eV from the original fitting. Then, we re-performed the least square fitting procedure using Eq. (10) on these down-selected microstates. The resulting new regression model of the vacancy binding energy for TiC and TaC show improvements from the original parametrizations based on the values of R^2 and \bar{R}^2 , which are over 0.99 in the new parametrization. Fig. 3 shows that the fitting residuals per vacancy from the new parametrization are within 0.08 eV in TiC and within 0.04 eV for TaC, which also indicates improvement.

The value and the corresponding p value of each parameter in Eq. (10) are listed in Table II. These results indicate that most of the fitted parameters have a confidence level of more than 90%. For those parameters with p values larger than 5%, their values are less than 0.05 eV, which is insignificant in the calculation of the total vacancy binding energy. We also note that values of ε_0 are close to zero, as anticipated, and confirm that our fitted microstates are indeed random and our fitting procedure is robust. The values of γ_1 can be interpreted as the statistical average over all our configurations of the first shell Me-C pairwise vacancy binding energy, which are close to

TABLE II. The coefficients, Eq. (10) and Fig. 2, for our CEM method obtained from the described fitting procedure (all units are in eV) and the corresponding p values. Powers of 10 are enclosed in brackets.

Parameter	Value (TiC)	p -value (TiC)	Value (TaC)	p -value (TaC)
ϵ_0	-8.61[-2]	2.29[-1]	5.43[-2]	9.74[-2]
α_2	2.17[-1]	2.08[-3]	8.89[-1]	1.03[-22]
α_4	-4.76[-1]	3.97[-7]	-3.14[-2]	2.93[-1]
α_6	-1.06[-1]	5.65[-2]	2.35[-1]	8.92[-9]
α_8	3.88[-2]	4.97[-2]	1.21[-1]	1.65[-2]
α_{10}	-1.93[-1]	5.03[-3]	-6.89[-2]	2.99[-2]
β_2	2.03[-1]	7.17[-8]	1.53[-1]	8.82[-8]
β_4	5.41[-1]	1.31[-19]	4.50[-1]	7.14[-18]
β_6	-4.32[-2]	6.89[-2]	-4.37[-2]	3.61[-3]
β_8	2.50[-1]	1.01[-5]	1.47[-1]	2.77[-6]
β_{10}	3.58[-2]	2.99[-1]	7.39[-3]	8.07[-1]
γ_1	-1.29	4.89[-42]	-1.69[-1]	1.17[-10]
γ_3	4.37[-2]	9.55[-3]	1.85[-1]	5.14[-16]
γ_5	-1.67[-1]	1.41[-5]	1.11[-2]	1.99[-2]
γ_9	4.43[-2]	9.57[-2]	-3.52[-2]	7.64[-2]
δ_{11}	-5.23[-1]	4.52[-2]	7.98[-2]	1.67[-1]
δ_{12}	-9.58[-1]	7.36[-3]	6.80[-2]	3.63[-2]
δ_{13}	-1.67[-1]	3.31[-2]	-1.58[-1]	2.96[-3]
δ_{14}	-1.03	1.80[-6]	-3.48[-2]	1.27[-1]
δ_{21}	8.91[-2]	1.29[-3]	-1.97[-2]	5.33[-1]
δ_{22}	9.64[-3]	5.18[-1]	-6.33[-2]	1.26[-2]
δ_{23}	-2.41[-2]	6.95[-1]	5.97[-2]	9.58[-3]
δ_{24}	-3.63[-1]	8.12[-3]	-1.52[-1]	2.32[-3]
δ_{31}	-7.16[-2]	2.21[-3]	-1.91[-2]	9.77[-2]
δ_{32}	-4.24[-1]	2.45[-6]	-3.22[-1]	2.80[-8]
δ_{33}	5.13[-2]	5.91[-1]	-6.11[-3]	6.03[-28]
δ_{34}	3.07[-1]	5.59[-4]	9.39[-3]	2.13[-2]

$E_{vb}[(\text{Me-C})_{1\text{st}}]$ obtained directly from our DFT calculations. Similarly, the statistical values for the C-C pairwise vacancy binding energy, β_2 , β_4 , and β_6 , in TiC are close to the reported values in Razumovskiy's work [21] demonstrating that our model should correctly capture C-C vacancy repulsion. These parameters also highlight the differences in vacancy clustering between TiC and TaC. Specifically, the β_2 term represents the first shell C-C vacancy interaction, which is positive in both materials and therefore repulsive, but when compared to the nearest-neighbor Me-C interaction, γ_1 , we can see this value is relatively smaller in TiC than in TaC. This means that, in TiC, it will be much easier for the Me-C vacancy attraction to overcome the C-C vacancy repulsion, allowing a stronger tendency for vacancy agglomeration. These differences in TiC and TaC are quantitatively studied in our MC simulations as described in the next section.

C. Configuration-dependent model for vacancy motion

The NNM and CEM models can be used to estimate the formation energies of different vacancy microstates and a similar model must be created for vacancy migration. This is necessary because we must be able to estimate the migration energy barrier of the vacancies for any configuration that occurs during a kMC step. However, unlike vacancy formation energies, the computational setup and cost of vacancy

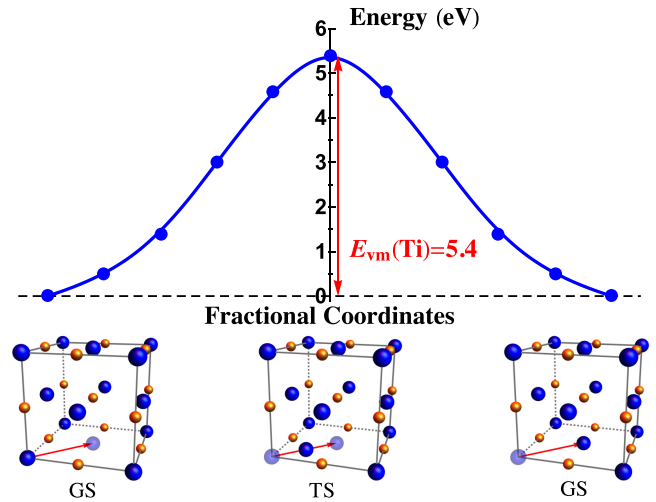


FIG. 4. The minimum energy path of a Ti vacancy migration in a 128 lattice-site supercell. The blue circles are the energy values directly computed from DFT and the maximum is the transition state (TS) representing the migration energy barrier. The corresponding initial, final, and transition states (a.k.a. the saddle point) are illustrated below the graph with the red arrow highlighting the migration path. Nine images, in addition to the two ground states (GS), were used to simulate the trajectory of the atoms.

migration barriers are both complicated and expensive, and thus conducting a random sample is infeasible. Therefore, to simplify our analysis, we consider only a limited number of vacancy jumps for specific configurations which are reasonably justified as representative of the system.

Before introducing the more general model, it is first critical to explain how we computed the migration energy barriers, E_{vm} , using DFT. In this work, we used the nudged elastic band (NEB) [45] method to locate the transition state along the diffusion path on the energy potential surface between two different microstates with the same number of atoms. Figure 4 shows an example of such a calculation where an isolated Ti atom is moving to a vacancy in its nearest neighbor shell along the path labeled with a red arrow. Along this path, we generated nine microstates in addition to the end points, or ground states (GS), using a linear interpolation scheme. The initial path was then relaxed using the NEB method so that the middle point converges on the transition state (TS) whose value represents the migration energy barrier.

However, we know from prior work that the migration barriers will vary with local atomic configuration, i.e., the energy will vary depending on the microstates used as the end points. Thus, we consider how this might happen for the migration of vacancies in a Me-C divacancy pair because the divacancy diffusion mechanism in TMCs is suggested in both experimental and computational works [21,46] and involves local atomic arrangement effects. A divacancy pair consists of Me and C vacancy bound in their nearest neighbor shells, which are circled in dashed lines as shown in Fig. 5. For the Me vacancy migration, there are 12 possible positions of the final state, which can be categorized into three independent cases. With respect to the C vacancy in the divacancy pair, the ending positions of the migrating Me vacancy are in

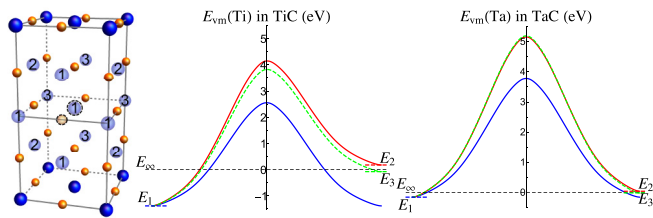


FIG. 5. The migration barriers of the Me vacancy in a divacancy pair. Vacancies in the divacancy pair are circled in dashed lines in the atomic configuration shown on the left. There are three possible ending points for the motion of a Me vacancy in a divacancy pair, which are labeled 1 through 3. The labeling also corresponds to a the motion of the coordination shell of the Me vacancy (after motion) with respect to the C vacancy. Thus the label three means the Me and C atom are in the third coordination shell after the migration. The energy along these three different diffusion paths is also shown with the blue curve for the migration from $1 \rightarrow 1$, red curve for the migration from $1 \rightarrow 2$, and dashed green curve for the migration from $1 \rightarrow 3$.

its first, second, and third shells, which are labeled with 1, 2, and 3, respectively. Therefore, the Me vacancy in a divacancy pair has three migrating paths, which are denoted as $1 \rightarrow 1$, $1 \rightarrow 2$, and $1 \rightarrow 3$.

We used the NEB method coupled with DFT to obtain the energy-barrier curves for those three diffusion paths, which are plotted relative to our reference energy E_∞ defined in Eq. (6). As shown in Fig. 5, the vacancy migration energy $E_{vm}(1 \rightarrow 2)$ is close to $E_{vm}(1 \rightarrow 3)$ but higher than $E_{vm}(1 \rightarrow 1)$. Similarly, we investigated the migration of the C vacancy in a divacancy pair and found that the vacancy migration energy $E_{vm}(C)$ in the diffusion path $1 \rightarrow 1$ is lower than those in the paths $1 \rightarrow 2$ and $1 \rightarrow 3$.

Therefore, we developed the so-called divacancy model (DM) for vacancy diffusion, in which the vacancy migration energy depends on the existence of other vacancies in its nearest neighbor shell. In the DM, the initial state and final state are denoted as Y if vacancies exist in its nearest neighbor and N if there is not. The migration of a vacancy is then categorized into four cases: YY, YN, NY, and NN. The vacancy migration energy for those four cases were then computed from DFT as:

$$E_{vm}^{YY} = E_{vm}(1 \rightarrow 1), \quad E_{vm}^{NN} = E_{vm}^{iso}, \quad (11)$$

$$E_{vm}^{YN} = [E_{vm}(1 \rightarrow 2) + E_{vm}(1 \rightarrow 3)]/2, \quad (12)$$

$$E_{vm}^{NY} = [E_{vm}(2 \rightarrow 1) + E_{vm}(3 \rightarrow 1)]/2. \quad (13)$$

Table III lists values of the vacancy migration energy in the divacancy model for TiC and TaC, which are used in kinetic Monte Carlo simulations to compute the rate of every possible vacancy jump in a bulk material.

In the paper by Razumovskiy *et al.* [21], the authors introduced a coordinated vacancy cluster mechanism that we have essentially reproduced here in our model. Those authors illustrated how a 1Ti-6C vacancy cluster might migrate in a coordinated fashion. Here, for illustrative purpose, we show in Fig. 6 how a 1Ti-4C cluster might migrate, in a coordinated

TABLE III. The values of the vacancy migration energy in the divacancy model (DM) (units in eV).

	E_{vm}^{YY}	E_{vm}^{YN}	E_{vm}^{NY}	E_{vm}^{NN}
Ti in TiC	3.95	5.39	3.96	5.40
C in TiC	2.31	3.58	2.15	3.79
Ta in TaC	3.98	5.35	5.19	5.31
C in TaC	3.82	3.73	3.56	4.00

fashion. However, we do not expect (and do not observe) these mechanisms as they are neatly shown in Fig. 6 or in Razumovskiy *et al.* [21]. This is because in our kMC simulations, as discussed below, the atoms that move are chosen at random and not in pre-determined coordinated fashion. Compared to metal vacancies, the lower migration energy of C vacancy and the larger number of C vacancies result in most of the atomic jumps being C atoms, which cause no net motion of the metal vacancy.

D. The vacancy jump frequency

The vacancy formation and migration energies are critical in understanding the self-diffusion problem, however it is still important to provide a reasonable estimate of the jump frequency ν_0 for our kMC simulations to accurately predict diffusion coefficients and activation energies. The vacancy jump frequency can be evaluated most simply using harmonic transition state theory (HTST) [47], which is based on the frequencies of vibration at the GS and TS of the migration path. These frequencies can be computed directly from the Hessian matrices at these two points. At the ground state, eigenvalues of the Hessian matrix have $3N - 3$ real frequencies and three rigid body modes corresponding to the translational motion of the supercell. At the transition state, there is at least one negative eigenvalue of the Hessian matrix because the total energy of the supercell is at a local maximum along the diffusion path as shown in Fig. 4. Thus, for our supercells, there are $3N - 3$ characteristic frequencies (ν_i^{GS}) in the ground state and at most $3N - 4$ characteristic frequencies (ν_i^{TS}) at the transition state. The vacancy jump frequency is then computed from

$$\nu_0 = \prod_{i=1}^{3N-3} \nu_i^{GS} / \prod_{i=1}^{3N-4} \nu_i^{TS}. \quad (14)$$

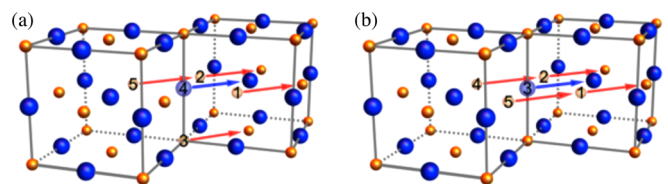


FIG. 6. A schematic plot of vacancy migration in the 1Ti-4C clusters. Subplots (a) and (b) represent two different initial configurations of the 1Ti-4C vacancy cluster. The transparent spheres represent the vacancies in the 1Ti-4C cluster. The numbers labeled on vacancies indicate the cluster jump sequence.

TABLE IV. The vacancy jump frequency computed from the partial Hessian matrix as described in the text (units in THz).

No. of atoms	$N = 63$	$N = 127$	$N = 215$
$\nu_0(\text{Ti})$ in TiC	10.39	11.69	11.52
$\nu_0(\text{C})$ in TiC	39.26	48.75	47.98
$\nu_0(\text{C})/\nu_0(\text{Ti})$	3.78	4.17	4.16
$\nu_0(\text{Ta})$ in TaC	4.36	3.63	3.51
$\nu_0(\text{C})$ in TaC	36.33	39.77	37.77
$\nu_0(\text{C})/\nu_0(\text{Ta})$	8.33	10.96	10.76

The calculation of the full Hessian is very expensive for large supercells, which prohibits the necessary size convergence studies to ensure accurate values of ν_0 . However, Eq. (14) can be extended to evaluate ν_0 from any partial Hessian matrix which includes the motion of the migrating atom and thus large supercells can be treated using the partial Hessian technique [48]. Here, we computed the jump frequency for single Me and C atoms as a function of supercell size for N equals 63, 127, and 215 as shown in Table IV. The partial Hessian used in our calculations only includes the motion of the atom and thus is a 3×3 matrix, which is necessary to prevent other negative frequencies which are associated with the atom moving into the local tetrahedral interstice.

For our kMC simulations, we used the values of ν_0 as determined from the simulation cells with $N = 215$ atoms. It is also interesting to note that the vibrations of the C atoms are much higher than the Me atoms, as would be expected since vibrational frequencies of harmonic oscillators scale inversely with the square root of the mass: $\omega \propto m^{-1/2}$. For comparison with experiments, we estimated the vibrational frequencies of TiC and TaC from ν_0 as:

$$\nu_0^*(\text{MeC}) = \frac{\sqrt{m_{\text{Me}}}\nu_0(\text{Me}) + \sqrt{m_{\text{C}}}\nu_0(\text{C})}{\sqrt{m_{\text{Me}}} + \sqrt{m_{\text{C}}}}, \quad (15)$$

which results in 23.6 THz and 10.5 THz for TiC and TaC, respectively. This is consistent with the reported Debye frequency from experiments [49]. This agreement is important to note since the simplest approximation of ν_0 is the Debye frequency of the solid. However, HTST allows us to specify the frequency of the Me and C atoms independently, which are needed in our simulations given the substantial differences in the masses of the elements and hence differences in their frequencies. These values of ν_0 , along with the aforementioned model of the migration energy barriers, allow us to conduct kMC simulations.

E. Monte Carlo simulations

The methodology above provides all of the necessary physical parameters to carry out the necessary Monte Carlo simulations to extract average vacancy formation energies and migration energies. To compute the average vacancy formation energies, we conducted Monte Carlo simulations using the Metropolis-Hastings algorithm (MMC) of $\text{Me}_{1-x}\text{C}_{1-y}$ titanium and tantalum carbides. The Metropolis-Hastings algorithm is a Markov chain Monte Carlo method [50], which

is used to obtain random samples from a large multidimensional system. In a bulk material with many vacancies, the total degrees of freedom is large and hence the implementation of the Metropolis-Hasting algorithm is appropriate. In our MMC simulations, the simulated system is a bulk B1-structured MeC material with a fixed Me and C vacancy concentrations x and y . Each simulation is carried out at a pre-determined temperature T that follows a standard MMC set of steps. First, the initial configuration of the simulated system is generated with a random vacancy distribution. Then, all possible vacancy jumps are listed and a random number is used to select one attempt. The energy change associated with this attempt, ΔE , is evaluated using Eq. (9) in the CEM as $\Delta E = E_{vb-\text{new}} - E_{vb-\text{old}}$. Then ΔE is used to calculate the acceptance probability of the attempt: $\rho = \exp(-\Delta E/k_B T)$. The attempt configuration is accepted if, after selecting a random number $u \in (0, 1)$, $u > \rho$ and is rejected if $u < \rho$. Once an attempt configuration is accepted, it becomes a new initial configuration and above steps are repeated.

Our kMC model was developed to simulate the time required to diffuse vacancies in our B1 MeC structure. In this model, we assume that only one vacancy can hop at a time which can be represented by a Poisson process and directly simulated using standard kMC methodologies. Initially, we generate a bulk configuration of the $\text{Me}_{1-x}\text{C}_{1-y}$ structure. From this configuration, all of the possible jump mechanisms and their energy barriers are enumerated using the aforementioned migration barrier models, i.e., the divacancy model (DM) as shown in Table III. The rates of all possible vacancy jumps are computed as:

$$r_i = \nu_0 \exp(-E_{vm}/k_B T), \quad (16)$$

where T is the constant simulated temperature and ν_0 is the appropriate vacancy jump frequency. The atomic migration event is selected randomly from a list of all possible events, each weighted by the rates at which the event can occur. Specifically, a random number is generated, $u_1 \in (0, 1)$, and multiplied by R_N , which is the cumulative total rate of all possible events. If $u_1 R_N$ falls in the range of $(R_{k-1}, R_k]$, then the k th event (jump) is carried out. Here, we are specifically using the cumulative rate function R_i defined as:

$$R_j = \sum_i^j r_i \quad (j = 1, 2, \dots, N). \quad (17)$$

The time of this event is then calculated based on another random number and the rate of the event as: $\Delta t = -\ln u_2/R_N$ where $u_2 \in (0, 1)$. Then, all of the possible jump possibilities have to be regenerated and the process is repeated.

In order to ensure the current configuration is independent of the initial configuration, we run a sufficient number of kMC steps to ensure that, on average, each vacancy hops 60 times. From this new starting point, we computed the diffusion coefficient using the Einstein diffusion equation [51]. For example, consider a bulk MeC material with m Me vacancies and n C vacancies where the i th Me vacancy with initial coordinates (x_{i0}, y_{i0}, z_{i0}) is located at (x_{i1}, y_{i1}, z_{i1}) for time $t = t_1$. The average displacement and average distance of all Me vacancies, noted as $\langle R(\text{Me}) \rangle$ and $\langle R^2(\text{Me}) \rangle$, respectively,

can then be calculated as:

$$\begin{aligned} \Delta x_i &= x_{i1} - x_{i0}, & \Delta z_i &= z_{i1} - z_{i0}, & \Delta z_i &= z_{i1} - z_{i0}, \\ \langle R(\text{Me}) \rangle &= \frac{1}{m} \sqrt{\left(\sum_{i=1}^m \Delta x_i \right)^2 + \left(\sum_{i=1}^m \Delta y_i \right)^2 + \left(\sum_{i=1}^m \Delta z_i \right)^2}, \\ \langle R^2(\text{Me}) \rangle &= \frac{1}{m} \sum_{i=1}^m (\Delta x_i^2 + \Delta y_i^2 + \Delta z_i^2). \end{aligned} \quad (18)$$

The diffusion coefficient of the Me vacancy $D(\text{Me})$ is then obtained from the Einstein relation:

$$6D(\text{Me})t_1 = \langle R^2(\text{Me}) \rangle. \quad (19)$$

The diffusion coefficient of the C vacancies can then be evaluated in a similar manner. The average value of D as evaluated using $\sim 10^3$ independent configurations generated in the kMC simulations, which correspond to 10 different simulations with 100 output steps for each simulation. Thus, the average D of those configurations is associated with the ensemble average of the vacancy migration energy, $\langle E_{vm} \rangle$, via the Arrhenius relation.

While the diffusion coefficient is the most important parameter computed from our kMC simulations, there are several other parameters that will provide invaluable insight into the diffusion of the C and Me vacancies. In kMC simulations of random walks, a scaling law is often used to characterize the type of random walk [52] that occurs. In a general random-walk process, the mean square displacement (displacement dispersion), $\langle \Delta R^2 \rangle$, is related to the number of steps in the random walk N_s as follows:

$$\langle \Delta R^2 \rangle_{N_s} = \langle R^2 \rangle_{N_s} - \langle R \rangle_{N_s}^2, \quad \langle \Delta R^2 \rangle_{N_s} \propto N_s^{2\nu}. \quad (20)$$

For an isotropic random walk, the exponent ν is about 0.5, otherwise the random walk is directional. To understand if our model results in a directional or isotropic random walk, we computed the mean square displacement and exponent ν from our kMC results. The other parameter computed during our MC simulations is the Warren-Cowley short range order (SRO) [53]. The SRO is a number from -1 to 1 which describes the local arrangement of atoms over a short distance, or in this case, vacancies. In this study, there are two types of vacancies: Me and C in a simulated system and thus we have different types of SRO. The short range order of the Me-C vacancies, denoted as $\text{SRO}(\text{C}|\text{Me})$, indicates the likelihood of the occurrence of C vacancies in the nearest neighbor of Me vacancies. In a configuration with a random distribution of vacancies, short range order is zero. A negative value of $\text{SRO}(\text{C}|\text{Me})$ suggests a tendency for C vacancies to migrate away from Me vacancies, whereas a positive SRO suggests a tendency to form Me- n C vacancy clusters. The SRO will provide quantitative assessments of the cluster mechanism and if or how it migrates through the lattice.

In both the MMC and kMC simulations, we chose to simulate $20 \times 20 \times 20$ repetitions of the conventional B1 unit cell with a total of 64 000 lattice sites. To understand compositional affects on our results, we simulated a bulk nonstoichiometric carbide $\text{Me}_{1-x}\text{C}_{1-y}$ with the Me vacancy concentration x varying from 0.002 to 0.006 (0.2% \sim 0.6%) and the C vacancy concentration y from 0.01 to 0.06 (1% \sim

TABLE V. The formation energy and migration energy for an isolated vacancy in TiC and TaC.

	Ti in TiC	C in TiC	Ta in TaC	C in TaC
E_{vf}^{iso} (eV)	7.44	0.15	2.57	0.21
E_{vm}^{iso} (eV)	5.40	3.79	5.31	4.00

6%). In all of our simulations, we chose the C vacancy concentration to be much larger than the Me vacancy concentration due to the substantial difference in vacancy formation energies and the fact that the carbides have a wide stoichiometry range including up to 50% vacancies in TiC. In the MMC and kMC simulations, each output configuration used for analysis was generated from a previous output configuration only after an average of 60 jumps per vacancy. For each bulk MeC simulation with a fixed vacancy concentration, 10 initial configurations were generated using different random seeds. Starting from each initial configuration, Monte Carlo simulations were carried out at a specific simulated temperature ranging from 2000 K to 2800 K in increments of 50 K. In each MMC run, a total of 10^5 output configurations were generated while a total 10^2 output configurations were generated for each kMC run. We ultimately have fewer kMC outputs due to the time it takes to generate the average 60 hops per Me vacancy in the kMC algorithm. The choice of these parameters, including the statistical justifications, can be found in the Appendix. The computer codes for MMC and kMC simulations in our study were written in FORTRAN 90 and run on linux workstations. To visualize and better understand the random vacancy hops in our kMC simulations, please refer to the supplemental video [54]. In order to ensure the viewer can see the vacancy migration clearly, in this video the simulated system only has 512 atomic sites with 1 Ti vacancy and 8 C vacancies, which is approximately 10^2 smaller than the simulated systems used in the analysis of this paper.

III. RESULTS AND DISCUSSION

Prior to discussing the results of our MMC and kMC simulations and the resulting ensemble averages of the formation and migration energies, it is informative to re-examine some of the results for specific microstates as they provide direct insight into the differences between TiC and TaC. Specifically, the values for isolated atom migration, both Me and C, are listed in Table V as obtained from our DFT simulations. These results verify that the activation energy of Me self-diffusion is much higher than that of C self-diffusion and thus Me self-diffusion is the rate limiting step in mass diffusion unless some type of cluster mechanism operates. It is worth pointing out that the activation energy for Ti self-diffusion is 12.84 eV, which is much higher than experimental data [12] as has been previously pointed and discussed in other works [20,21]. It is also worth noting that using this methodology, the activation energy for the self-diffusion of Ta atom is 7.88 eV, which is not particularly high when compared to experimental results of creep in TaC and much lower than that of TiC, suggesting that perhaps our hypothesis of differences between the group IVB and VB carbides is indeed correct.

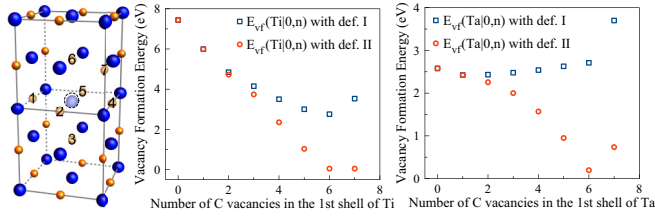


FIG. 7. The vacancy formation energy of Me atom as a function of the number n of nearest neighbor C vacancies. The Me vacancy is the transparent blue sphere that is enclosed in a dashed line and the potential C vacancies in its nearest neighbor are labeled 1 ~ 6. The values of E_{vf}^I , definition I, are computed from Eq. (7) and plotted in blue squares while those with definition II are plotted in red circles. Note that for the number of C vacancies being 2, 3, and 4, the data points are the average of all possible microstates.

Razumovskiy *et al.* [21] suggested that the activation energy for Ti self-diffusion can be lowered when Ti vacancies are surrounded by C vacancies, forming vacancy clusters. To verify that our models are consistent with Razumovskiy *et al.* and to provide a better understanding of the vacancy clustering mechanism, we computed the formation energy of a Me atom for both compounds, TiC and TaC, using both of our definitions given above for E_{vf}^I and E_{vf}^{II} in a cluster setting. The results of our calculations, plotted as a function of C vacancies surrounding the Me vacancy, are shown in Fig. 7 where each data point is an average of all possible microstates. If we consider our definition I, which is consistent with Razumovskiy *et al.* [21], we see that the formation energy of the Ti vacancy with six C vacancies in its nearest neighbor is 2.76 eV. However, the vacancy formation energy of Ta is nearly independent of the number of C vacancies in its nearest neighbor. This suggests that the vacancy-cluster mechanism in TaC is not particularly energetically favorable, supporting our hypothesis of differences in the two compounds. Our results for definition II, which is used in our MMC simulations, are shown alongside this data to demonstrate the differences in the two definitions.

The formation of a single metal vacancy in TiC, which presumably has a stronger overlap of the metal and carbon electron clouds, requires more energy to redistribute these bonds when the metal atom is removed. This leads to a higher metal vacancy formation energy for a single Ti vacancy, as shown in Table V. Similarly, the formation of isolated metal and carbon vacancies requires more energy to redistribute the overlapped electron clouds as compared to the formation of a bound metal-carbon vacancy pair. This is because in the bound vacancy pair, some of those bonds no longer exist and thus do not require energy to rearrange. Since this redistribution is costlier in TiC, the binding energy of a metal and carbon vacancy is larger in magnitude in TiC than it is in TaC. This provides further evidence that the bonds in TiC are more directional in nature than in TaC, which is consistent with findings in our previous work [17,23,55] comparing these two systems in other contexts.

A. Ensemble average of the Me vacancy formation energy

In order to evaluate the ensemble average of the vacancy formation energy, $\langle E_{vf} \rangle$, MMC simulations were carried out

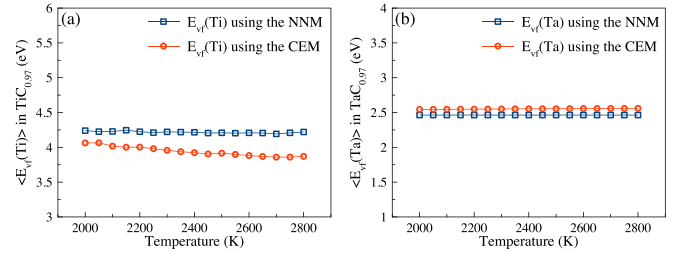


FIG. 8. The ensemble average of the Me vacancy formation energy from the MMC simulations at different temperatures: The blue markers denote $\langle E_{vf}(\text{Me}) \rangle$ values evaluated using the nearest neighbor model while the red markers denote $\langle E_{vf}(\text{Me}) \rangle$ evaluated using the cluster expansion method. (a) $\langle E_{vf}(\text{Ti}) \rangle$ in $\text{TiC}_{0.97}$; (b) $\langle E_{vf}(\text{Ta}) \rangle$ in $\text{TaC}_{0.97}$.

in the canonical ensemble, NVT , at different constant temperatures T without any Me vacancies to sample all potential Me vacancy sites in the presence of C vacancies. As the formation energy has the potential, due to clustering, to depend on the C concentration, we examined different C concentrations, i.e., MeC_{1-y} as a function of y up to 0.06 (6%). The Me vacancy formation energy can be computed as an ensemble average:

$$\langle E_{vf}(\text{Me}) \rangle = \frac{\sum_{i=1}^{n_{\text{out}}} \sum_{j=1}^{N/2} E_{vf}(\text{Me}) e^{-E_{vf}(\text{Me})/k_B T}}{\sum_{i=1}^{n_{\text{out}}} \sum_{j=1}^{N/2} e^{-E_{vf}(\text{Me})/k_B T}}, \quad (21)$$

where N is the total number of lattice sites and n_{out} is the total number of output configurations from the MMC simulations. The denominator in Eq. (21) represents the total probability of forming the Me vacancy at all Me atom positions, which is the partition function. We evaluated E_{vf} at each Me atom position using two different models: the nearest-neighbor model (NNM) and the cluster expansion method (CEM). Using the NNM, the value of $E_{vf}(\text{Me})$ at the specific position was chosen from Table II by only taking the number of C vacancies in its nearest neighbor shell into consideration. Using the CEM, $E_{vf}(\text{Me})$ was computed from Eq. (8), in which the energy of microstates $E[N - m - n - 1, m + 1, n]$ and $E[N - m - n, m, n]$ was evaluated by summing over local vacancy configurations as shown in Fig. 2.

The temperature dependence of $\langle E_{vf}(\text{Me}) \rangle$ as computed by both our models is shown in Fig. 8 for both TiC and TaC. In TaC, we can see that both models are in close agreement and do not depend on temperature. The slight differences observed here are due to the different energetics produced by both models and are very close to the formation energy of an isolated Ta vacancy, but that is not a particularly meaningful statement due to the flat nature of the formation energy curve with respect to the number of bound C vacancies.

The case of Ti is much more interesting. First, we note there is a larger difference between the magnitude of the formation energies predicted by the NNM and CEM models. Second, we note that the CEM model exhibits temperature dependent vacancy formation energies such that the formation energy decreases with increasing temperatures, while the NNM has no temperature dependence. This difference originates in how the models handle C-C vacancy-pair repulsion. The CEM model demonstrates, as does the C-C vacancy binding energies computed previously [21], that the C vacancies

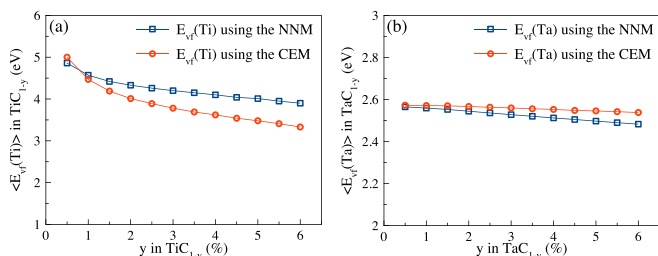


FIG. 9. The ensemble average of the Me vacancy formation energy from the MMC simulations in MeC with different C-vacancy concentrations: The blue markers denote $\langle E_{vf}(\text{Me}) \rangle$ evaluated using the nearest neighbor model while the red markers denote $\langle E_{vf}(\text{Me}) \rangle$ evaluated using the cluster expansion method. The values in all cases are then averaged over the whole investigated temperature range (2000 ~ 2800 K). (a) $\langle E_{vf}(\text{Ti}) \rangle$ in TiC_{1-y} and (b) $\langle E_{vf}(\text{Ta}) \rangle$ in TaC_{1-y} .

are generally repulsive in the absence of Ti vacancies. Thus, at higher temperatures, entropy allows for a higher probability of forming C vacancy clusters in which a Ti vacancy can form. This, in turn, lowers the vacancy formation energy giving rise to the temperature dependence observed in Fig. 8. When computing $\langle E_{vf} \rangle$ at every Me atom position, these C-C interactions are included in the CEM model and absent in the NNM model, and thus the CEM has a temperature dependence whereas the NNM does not.

Figure 9 shows the values of $\langle E_{vf}(\text{Me}) \rangle$ averaged over temperatures from 2000 K to 2800 K as a function of C concentration for both TiC and TaC. The Me vacancy formation energy decreases steeply in the TiC between 0.5% and 2% ($y = 0.005 \sim 0.02$) and then decreases at a nearly constant rate of 0.6 eV between 2% and 6% ($y = 0.02 \sim 0.06$). The Me vacancy formation energy in TaC shows a more constant and shallower decrease in formation energy over all of the simulated composition range. This can be attributed to the lower binding energy of vacancies in TaC as previously discussed. While our simulations do not extend beyond $y = 0.06$, we suspect that $\langle E_{vf}(\text{Me}) \rangle$ will gradually decrease towards the minimum value in Table II, definition I, which is 2.76 eV in TiC and 2.42 eV in TaC near the lower limit of their experimental composition ranges. The composition effect arises from the larger number of C vacancies present in the system, which increase the probability of the C atoms clustering and thus lower the Me vacancy formation energy. To facilitate direct comparisons with experimental data, we extracted the Me vacancy formation energy at the $\text{MeC}_{0.97}$ composition, which are: $\langle E_{vf}(\text{Ti}) \rangle = 3.87$ eV and $\langle E_{vf}(\text{Ta}) \rangle = 2.56$ eV, which again are an average between 2000 K and 2800 K.

B. Formation of Me-*n*C vacancy clusters

The ensemble average of the vacancy formation energy described above was computed in the absence of Me vacancies because we expect that, due to their high formation energies, statistically they should be absent. However, this approach does not provide insights into the average cluster size that should be present during migration. To provide further insight into this phenomena, we conducted MMC simulations for

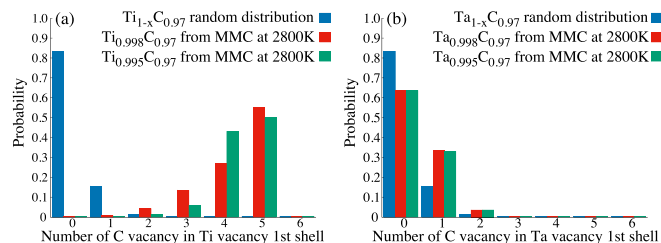


FIG. 10. The fraction of Me-*n*C vacancy clusters that form in the MMC simulations at 2800 K using the cluster expansion method, illustrating the effect of the percentage of Me vacancies on the types of cluster that form. The blue bars represent the fraction of the vacancy clusters that form in $\text{Me}_{1-x}\text{C}_{0.97}$ with a random distribution of vacancies. The red bars represent the fraction of the vacancy clusters that form in $\text{Me}_{0.998}\text{C}_{0.97}$ from our MMC simulations. The green bars represent the fraction of the vacancy clusters that form in $\text{Me}_{0.995}\text{C}_{0.97}$ from our MMC simulations. This is shown for (a) Ti-*n*C and (b) Ta-*n*C vacancy-cluster formation.

$\text{Me}_{1-x}\text{C}_{1-y}$ compositions in which we have a finite number of Me and C vacancies.

For a random distribution of vacancies, which is the same as a system with zero binding energy between all the vacancies, the probability of forming a Me-*n*C vacancy cluster is $C(6, n)y^n(1-y)^{6-n}$, where C denotes the number of combinations. This distribution is shown in Figs. 10 and 11 as the blue bars for $\text{Me}_{1-x}\text{C}_{0.97}$ compositions, which demonstrates that the most probable configuration is the unclustered Me vacancy with $n = 0$. Figure 10 shows the distributions that result from running our MMC code at 2800 K for TiC and TaC at two different compositions, $\text{Me}_{0.998}\text{C}_{0.97}$ and $\text{Ti}_{0.995}\text{C}_{0.97}$. The results for TaC at both compositions shows a nearly random distribution, indicating only a slight tendency for clustering. The fraction of clusters with $n \geq 2$ is less than 5%, demonstrating that the distribution is essentially unaffected by the number of Me vacancies. The increase in the number of Ta-1C clusters relative to the random distribution is related to the small binding energy of Ta and C vacancies in the nearest neighbor shell.

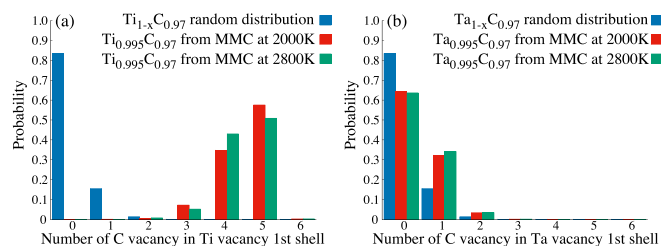


FIG. 11. The fraction of Me-*n*C vacancy clusters that form in MMC simulations for $\text{Me}_{0.995}\text{C}_{0.97}$ using CEM (cluster expansion method) at different temperatures. The blue bars represent the fraction of the vacancy clusters that would form in $\text{Me}_{1-x}\text{C}_{0.97}$ with a random vacancy distribution. The red bars represent the fraction of the vacancy clusters that form during our simulations at 2000 K and the green bars represent the fraction of the vacancy clusters that form at 2800 K. This is shown for (a) Ti-*n*C vacancy-cluster formation and (b) Ta-*n*C vacancy-cluster formation.

Contrary to the case in TaC, we do see obvious evidence of clustering in TiC as a result of the high Me-C vacancy binding energy (-1.29 eV) and the continual decrease in formation energy with cluster size shown in Fig. 7. In $\text{Ti}_{1-x}\text{C}_{0.97}$, about 90% of the Ti vacancies exist in Ti-4C and Ti-5C vacancy clusters. When the concentration of Ti vacancies lies between 0.2% to 0.6% ($x = 0.002 \sim 0.006$), the Ti-5C vacancy cluster is the most probable state for a Ti vacancy as computed from our MMC results. Above 0.6%, and up to our simulated maximum of 3% Ti vacancies, the most probable location of a Ti vacancy is in a Ti-4C vacancy cluster. This means that the favorability of a Ti- n C cluster depends on the ratio between the number of Ti vacancies and C vacancies. The more Me vacancies, the less C vacancies surround them, which simply reflects the number of C vacancies available to form a cluster. However, the distribution of Ta- n C vacancy clusters does not change with respect to the Ta vacancy concentration, which is due the low favorability of forming vacancy clusters in TaC. If we now consider a fixed composition $\text{Me}_{0.995}\text{C}_{0.97}$, the formation of Me- n C vacancy clusters redistributes at higher temperatures as shown in Fig. 11. This is indeed expected since the acceptance rate in our MMC simulations obeys the Boltzmann distribution.

Given the emphasis placed on the Ti-6C vacancy cluster proposed by Ref. [21], we now turn our attention to this cluster in the context of our MMC results. All our simulations, for $\text{Ti}_{1-x}\text{C}_{1-y}$ with $x = 0.002 \sim 0.03$ and $y = 0.01 \sim 0.06$, show that the probability of a Ti vacancy occurring in a Ti-6C vacancy-cluster formation is less than 10^{-4} . For example, in $\text{Ti}_{0.995}\text{C}_{0.97}$, the ratio of the number of Ti vacancies and that of C vacancies is 1:6 providing ample number of C vacancies for which to form Ti-6C vacancy clusters. However, from our simulations at 2800 K, there are only 184 Ti-6C vacancy clusters among the total 1.6×10^7 vacancy clusters in the whole catalog of our simulation results. Thus, even when the vacancy binding energy favors the formation of Ti-C vacancy clusters, the probability of forming a Ti-6C vacancy cluster in $\text{Ti}_{1-x}\text{C}_{1-y}$ with $x \leq 0.03$ and $y \leq 0.06$ is negligible. This suggests that the Ti-6C vacancy cluster proposed by Razu-movskiy *et al.* [21] does not contribute to the migration of Ti vacancy clusters in low C concentration titanium carbides. However, we cannot rule out that it is important near compositions of $\text{TiC}_{0.5}$, but it appears irrelevant to the experimentally measured Ti diffusion activation energies.

C. The vacancy migration energy

In order to investigate the migration of vacancies and compute the ensemble average of the vacancy migration energy, we conducted kMC simulations on TiC and TaC with both Me and C vacancies, i.e., $\text{Me}_{1-x}\text{C}_{1-y}$ with $y = 0.03$ and $x = 0.002 \sim 0.006$. Example diffusivity plots from our simulations are shown in Fig. 12 for Ti and C migration in TiC as well as Ta and C migration in TaC. Since the diffusivity is related to the ensemble average of the migration energy through the Arrhenius relation:

$$D \propto \exp(-\langle E_{vm} \rangle / k_B T), \quad (22)$$

the migration energies can be extracted from a linear regression of the semilog plots shown in Fig. 12. In addition to

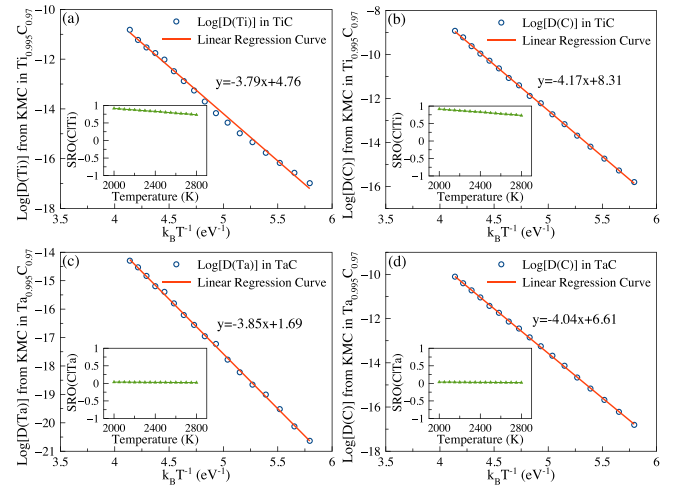


FIG. 12. Semilog plots of diffusion coefficients versus temperatures from the kMC simulations of $\text{Me}_{0.995}\text{C}_{0.97}$. The blue markers are the data obtained from the kMC simulations and the red lines represents the linear regression curve. In the subplots, the SRO(C|Ta) parameters at temperatures from 2000 K to 2800 K are shown. This is for: (a) Ti diffusion in TiC, (b) C diffusion in TiC, (c) Ta diffusion in TaC, (d) C diffusion in TaC.

the diffusivity, the subfigures in Fig. 12 show the associated Warren-Cowley short range order parameter for C vacancies with respect to Me vacancies, i.e., $\text{SRO}(\text{C}|\text{Me})$.

The data shown in Fig. 12 for the ensemble average of the vacancy migration energies in $\text{Ti}_{0.995}\text{C}_{0.97}$ are 3.79 eV and 4.17 eV for Ti and C, respectively, and 3.85 eV for Ta and 4.04 eV for C in $\text{Ta}_{0.995}\text{C}_{0.97}$. Thus, we can see that the migration energy barriers for both C and Me atoms of the two TMCs are quite similar. However, we note that the parameters $\text{SRO}(\text{C}|\text{Me})$ in the two materials are indeed different. The $\text{SRO}(\text{C}|\text{Me})$ for Ti vacancy migration is above 0.75, indicating that the Ti vacancies are surrounded by four or five C vacancies and therefore consistent with our MMC results. Of course, the $\text{SRO}(\text{C}|\text{Me})$ decreases with increasing temperature, suggesting that with increasing temperature the C vacancies are less likely to be tightly bound to the Ti vacancy as already noted above.

We note that $\langle E_{vm}(\text{Ti}) \rangle$ in TiC is 0.15 eV smaller than the lowest Ti vacancy migration energy in the divacancy model $E_{vm}^{YY}(\text{Ti})$. This arises due to an uncertainty of 0.19 eV in the linear regression, suggesting that the $E_{vm}^{YY}(\text{Ti})$ barrier controls Ti vacancy diffusion. Hence, this clearly demonstrates that Ti vacancies move primarily when both its starting and ending configuration have C vacancies. However, $\langle E_{vm}(\text{C}) \rangle$ in TiC is 0.3 eV larger than the highest C vacancy migration energy (larger than our fitting uncertainty) in the divacancy model $E_{NN}(\text{C})$. The reason is that the jumping rate of C vacancies is much higher than that of Me vacancies. Therefore, once the Ti- n C vacancy cluster forms, most of the C jumps are around Ti vacancies and thus the C vacancy migration is constrained, resulting in a higher effective activation energy. In contrast, every jump of a Ti vacancy occurs in a cluster, and diffuses randomly since there are many more C vacancies than Me vacancies.

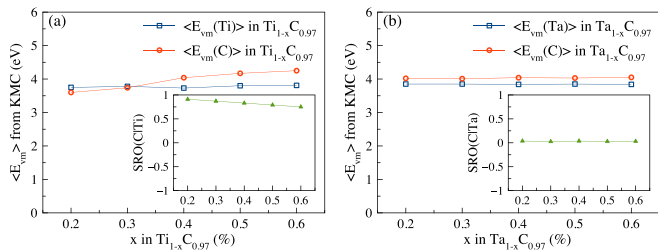


FIG. 13. The ensemble average of the vacancy migration energy for $Me_{1-x}C_{0.97}$ plotted as a function of the Me vacancy concentration x . The blue lines with markers denotes $\langle E_{vm}(Me) \rangle$ and the red line with markers denotes $\langle E_{vm}(C) \rangle$. In the subplot, the values of SRO(C|Me) are also plotted against the Me vacancy concentration x . (a) in TiC; (b) in TaC.

In the case of TaC, the $\langle E_{vm}(Ta) \rangle$ is similarly 0.13 eV lower than the lowest Ta vacancy migration barrier $E_{vm}^{YY}(Ta)$, but again is within our linear regression error. The migration barrier for C in TaC is essentially the same as the largest C vacancy migration barrier $E_{vm}^{NN}(C)$. The SRO(C|Me) for TaC is positive but small, suggesting that most of the Ta vacancies either have one or zero bound C vacancies. However, the low activation energy in Ta vacancy migration suggests that they move in a way that is coordinated by C vacancies. We interpret these results to suggest that the Ta vacancy typically migrates with one C vacancy in its nearest neighbor to another lattice site with a nearest-neighbor C vacancy, but not in the way of being surrounded by multiple C vacancies like in TiC.

We also studied the Me vacancy composition on the vacancy migration energy, $\langle E_{vm} \rangle$, to ensure that our choice of the number of Me vacancies is not affecting our results. The vacancy migration energy, $\langle E_{vm} \rangle$, was computed for different values of x in the $Me_{1-x}C_{0.97}$ compounds from the linear regression method shown in Fig. 12. This average migration energy barrier and the average SRO(C|Me) for temperatures from 2000 K to 2800 K are shown in Fig. 13. These results indicate that $\langle E_{vm}(Me) \rangle$ is independent of the Me vacancy concentration in both TiC and TaC. In $Ta_{1-x}C_{0.97}$, both $\langle E_{vm}(Ta) \rangle$ and $\langle E_{vm}(C) \rangle$ do not depend on the Me vacancy concentration because there is no aggregation of Ta and C vacancies, which can also be explained from the values of SRO(C|Ta). In $Ti_{1-x}C_{0.97}$, there is a slight dependence of $\langle E_{vm}(C) \rangle$ on the Ti vacancy concentration, which increases with increasing Ti vacancy concentration. In addition, there is a corresponding decrease in SRO(C|Ti). We can attribute this to the ratio of C vacancies to Ti vacancies. As we increase the number of Ti vacancies, these vacancies should attract C vacancies, reducing the coordination of Ti vacancies overall, as seen in the SRO(C|Ti). This further constrains the motion of the C atoms, which causes the C migration energy to increase slightly.

To better understand the nature of the vacancy diffusion mechanisms as random walks, we extracted the random walk exponents for all four vacancy types: Ti and C in TiC and Ta and C in TaC. The log-log plots of $\langle \Delta R \rangle$ with respect to the number of vacancy jumps N is shown in Fig. 14, where $\langle \Delta R \rangle$ is the square root of the displacement dispersion in Eq. (20): $\langle \Delta R \rangle \equiv \langle \Delta R^2 \rangle^{1/2}$. In all the cases, these results exhibit

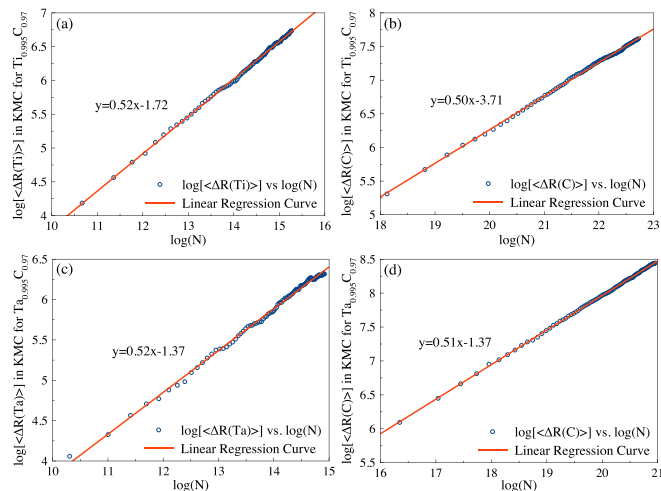


FIG. 14. Log-log plots of $\langle \Delta R \rangle$ versus N demonstrating the scaling law in the kMC simulations of $Me_{0.995}C_{0.97}$ at 2800 K. (a) Ti diffusion in TiC; (b) C diffusion in TiC; (c) Ta diffusion in TaC; (d) C diffusion in TaC.

a linear relationship with a slope of ν , which was extracted via linear regression, that varies between 0.48 and 0.52. This means that both the Me vacancy migration and the C vacancy migration are isotropic and random for both TiC and TaC, irrespective of vacancy concentrations and temperatures. This clearly demonstrates that the vacancy cluster motion mechanism does not affect the isotropic nature of diffusion in these materials.

D. Temperature effects on the activation energy for the self-diffusion

In DFT calculations, the computed total energy for a microstate is an approximation of the many-body problem and is formally evaluated at zero Kelvin. Thus, when the vacancy formation energy and migration barriers are computed in DFT as done here and in previous work, this activation energy, $Q_a = E_{vf} + E_{vm}$, is similarly evaluated at zero Kelvin. However, in experiments the activation Gibbs free energy (Q_a^*) is measured, which can be related to the value computed in DFT as:

$$Q_a^* = Q_a - T(\Delta S_{cf} + \Delta S_{vib} + \Delta S_{el}) + p\Delta V, \quad (23)$$

where ΔS_{el} is the electronic entropy, ΔS_{cf} is the configurational entropy, and ΔS_{vib} is the vibrational entropy [56]. In this study, the ensemble average of the vacancy formation energy and migration energy were obtained using Monte Carlo simulations at different temperatures and therefore included the effects of configurational entropy. Thus, there are three factors that need further investigation: the electronic entropy ΔS_{el} , the entropy of phonons ΔS_{vib} , and the thermal expansion effects of the MeC compound, ΔV .

At a finite temperature, the electronic entropy has two forms: the thermal smearing of electronic states around Fermi level [57] and the configurational entropy associated with the distribution of localized and unlocalized charges [58]. In TiC and TaC, the electrons are localized to form covalent bonds or covalent-metallic bonds. Previous studies on the

TABLE VI. Values of the activation energy for the self-diffusion obtained in experiments (Expt.) and in Monte Carlo simulations (MC) (units in eV).

	TiC		TaC ^a	
	$Q_a(\text{Ti})$	$Q_a(\text{C})$	$Q_a(\text{Ta})$	$Q_a(\text{C})$
Expt.	7.58 ± 0.16^b	$4.09^c(1.15 \sim 4.59)^d$		$(3.69 - 4.34)^e$
MC	7.66 ± 0.19	4.32 ± 0.10	6.41 ± 0.15	4.38 ± 0.10

^aNo experimental data found for the direct measurement of $Q_a(\text{Ta})$ for the self-diffusion in TaC.

^bTiC_{0.67-0.97} in 2193 ~ 2488 K; Ref. [12].

^cTiC_{0.97} in 1723 ~ 2553 K; Ref. [9].

^dTiC_{0.4-0.89}; Ref. [10], Ref. [11].

^eTaC_{1-y}; Ref. [13]; Ref. [14]; Ref. [15].

band structure in TiC [59,60] and TaC [61] indicate that the peaks are several eV below the Fermi level, which means the number of states within $\pm k_B T$ of the Fermi level are relatively small. Therefore, the electronic entropy contributions to the activation free energy in TiC and TaC should be negligible.

The entropy contribution due to phonons, ΔS_{vib} , and lattice thermal expansion, ΔV , can be evaluated using density functional perturbation theory [62,63]. Alternatively, Razumovskiy *et al.* [21] performed finite temperature DFT calculations of TiC and they found that, from 0 K to 2000 K, the lattice constant change was less than 1% and the vibrational entropy ΔS_{vib} lowered the vacancy formation energy only 0.12 eV, which is generally small comparable to E_{vm} and E_{vf} . Sun *et al.* [22] also performed the finite temperature DFT calculations and came to the same conclusion. Therefore, all three terms, ΔS_{vib} , ΔS_{el} , and ΔV in Eq. (23), are negligible. In other words, the ensemble average of the activation energy $\langle Q_a \rangle = \langle E_{\text{vf}} \rangle + \langle E_{\text{vm}} \rangle$ in our work, which includes the configurational entropy, should be a good approximation to the experimental data.

To be consistent with experiments in TiC, we report the average values of $\langle Q_a \rangle$ in Me_{0.995}C_{0.97} from 2000 K to 2800 K, which are listed in Table VI. In these calculations, the vacancy formation energy for an isolated C is used for $\langle E_{\text{vf}}(\text{C}) \rangle$. As listed in Table V, the vacancy formation energy for an isolated C is less than 0.2 eV, which is much smaller than the Me vacancy formation energy and therefore it is sufficient to assume that the C atoms can spontaneously form in the calculation of the Me vacancy formation energy. The uncertainties in the reported activation energies come from convergence tests in DFT and the fitting errors in the linear regression.

For TiC, we compare our simulation results to the listed experimental data [9,12] of the self-diffusion activation energy since the temperature range and vacancy concentration in those measurements are close to our simulation conditions. Other reported experimental data for the self-diffusion $Q_a(\text{C})$ in TiC with higher C vacancy concentrations are mentioned in parenthesis. For TaC, the data for the C self-diffusion activation energy are listed in parenthesis because the activation energies are extracted from diffusion couples and represent averages of the homogeneity range of B1 TaC_{1-y}. Unfortunately, there is no data on the self-diffusion of Ta in TaC. Assuming the activation energy measured for creep at high

temperature is close to the activation energy for bulk diffusion, we can refer to the experimental data obtained from the tensile creep test [6], which is 7.2 ± 1.3 eV and close to our simulation results of $Q_a(\text{Ta})$. However, it is not as good an agreement with the bending creep tests by Smith *et al.* [7], but there is a lack of a direct physical link between the activation energies extracted from those bending creep experiments and the activation energy for diffusion and thus a disagreement is understandable. Therefore, from Table VI, the activation energy for self-diffusion obtained in our statistical study shows good agreement with experimental data.

Finally, it was suggested in a previous theoretical study [64] that the activation energy for Ti self-diffusion decreases as the C vacancy concentration increases, which is also observed in our statistical results. However, this vacancy-composition dependence of $Q_a(\text{Ti})$ in TiC was not found in experimental measurements [12,65] due to the large experimental uncertainty.

IV. CONCLUSIONS

In this paper, the formation and migration of vacancies in TiC and TaC were investigated at different scales, from electronic structure calculations to Monte Carlo simulations. Using the energetics parameterized from DFT, Monte Carlo simulations were used to determine the ensemble averages of the vacancy formation energy and vacancy migration energy. These values were found to be in reasonable agreement with experimental results.

Our DFT simulations demonstrate that the energetics of vacancy formation in TiC and TaC are quite different. DFT energetics suggest it is very difficult to form isolated Ti vacancies, but the vacancy formation energy for an isolated Ta vacancy is considerably lower. In addition, we found that the binding energy of C vacancies to Ti vacancies is quite high, -1.45 eV, while the binding energy between a Ta and C vacancy is considerably lower, -0.16 eV. Similarly, the vacancy formation energy of Me vacancies in both Ti-*n*C and Ta-*n*C clusters were calculated confirming that the formation energy for Ti vacancies decreases with the increasing number of bound vacancies. We demonstrated that such a trend is nearly absent in TaC. All of these DFT simulations demonstrate that

TiC has a much stronger preference to form vacancy clusters than TaC.

Our MMC simulations further provide evidence of the nature of clustering in these two materials. The statistical number of vacancies around both Ti and Ta vacancies were computed at different compositions and temperatures with the trends generally agreeing with our DFT simulations. However, in this case we can directly determine the relative probability of forming different cluster sizes. In TiC, we found that most of the Ti vacancies are part of Ti-4C and Ti-5C clusters, with so few Ti-6C clusters that they can be ignored. This is in direct contrast to the importance of the Ti-6C cluster put forth by Razumovskiy *et al.* [21] in which they proposed this was the most important microstate. In the case of Ta vacancies, our simulations demonstrate that these vacancies tend to form either as isolated vacancies or as part of Ta-1C bound divacancies.

The kMC simulations confirm our MMC results with regards to the nature of C vacancy clusters in the migration of Ti and Ta vacancies. The ensemble average migration energies of the Me vacancy are associated with its migration in between states that are both bound to C vacancies. In TiC, this is easily achieved due to the large number of C vacancies in which it is surrounded. However, this result for Ta vacancies suggest that their motion is primarily coordinated by C vacancies as well even if it is not surrounded by a large number of them. Thus we can conclude that the isolated Ta vacancies, while more prevalent, contribute less to the diffusion of Ta vacancies. Finally, the values of the ensemble-average activation energy $\langle Q_a \rangle$ obtained in our MC simulations include configurational entropy and are close to experimental data in both TiC [9,12] and TaC [5–7].

ACKNOWLEDGMENTS

This work utilized the RMACC Summit supercomputer, which is supported by the National Science Foundation (Awards No. ACI-1532235 and ACI-1532236), the University of Colorado Boulder and Colorado State University. The RMACC Summit supercomputer is a joint effort of the University of Colorado Boulder and Colorado State University. G.B.T. recognizes NSF-DMR-2026760 and C.R.W. recognizes NSF-DMR-2026766 for additional support.

APPENDIX: STATISTICAL REQUIREMENTS IN MONTE CARLO SIMULATION

In any Monte Carlo simulation, the simulation should converge to the correct statistical solution after sufficient, and perhaps infinite, time. However, running Monte Carlo simulations are computational expensive and therefore it is important to reduce the number of samples down to those that correctly represent the system response without excessive simulation time. In this Appendix, we justify the values of our two MC simulations.

First, it is important to ensure that the simulated cell sizes in our simulations are of sufficient size. If we consider m Me vacancies and n C vacancies in the B1 structure, the statistical distribution of the vacancy displacements from their

initial configurations should be normally distributed with a zero mean value as m diverges. However, in a system with a finite number of vacancies, the distribution is defined by the students t distribution [66]: $t(m-1)$. To correctly reproduce the normal distribution statistics, the number m must be larger than 30 so that the students t distribution sufficiently represents the normal distribution, which defines the smallest acceptable simulations cell. Thus, our Monte Carlo simulation cells at the smallest Me vacancy concentration must have at least 30 vacancies.

Second, it is important to establish the number of Monte Carlo steps necessary to take between each output step to ensure that the configurations used in the analysis are independent. As noted in the methodology section, we chose this output to occur after each vacancy moves 60 times (on average). This criterion was chosen in order to ensure that the binomial distribution, which represents the jump probability, converges to the normal distribution. To understand our rationale, note that the i th vacancy can jump in one of 12 directions, which corresponds to all of the possible $\langle 110 \rangle$ directions in the B1 structure. Since the jumps in each direction are isotropic and independent, after n_j jumps the displacement in the j th direction, \vec{R}_{ij} , should satisfy the binomial distribution [67] $\vec{R}_{ij} \sim B(n_j, p)$ where $p = 1/12$. One widely used convention that ensures the normal approximation of the binomial distribution [68] $B(n, p)$ is $np \geq 5$, which leads to the requirement of $n_j \geq 60$ for our 12 directions. Thus, we chose to ensure that all of our vacancies have jumped at least 60 times to ensure we have achieved independent or random atomic configurations in our MC simulations.

In our kMC simulations, the values of $R^2(\text{Me})$ for all m Me vacancies were computed in all of the output configurations, n_{out} , using Eq. (18), which satisfies the chi-square distribution [69]: $R^2(\text{Me}) \sim \chi^2(m)$. To obtain the vacancy migration energy, the diffusion coefficient D is computed from Eq. (19) as the average in all n_{out} configurations:

$$D(\text{Me}) = \frac{1}{n_{\text{out}}} \sum_{k=1}^{n_{\text{out}}} \frac{\langle R^2(\text{Me}) \rangle_k}{6t_k}. \quad (\text{A1})$$

Studies [68] show that the sample mean $D(\text{Me})$ converges to the normal distributions when $n_{\text{out}} \geq 50$, which sets the minimum number of output configurations that can be used.

As noted above, each independent configuration was generated after an average of 60 jumps per vacancy: $n_j = 60$. Thus, our MMC and kMC models used $n_{\text{out}} = 10^5$ and $n_{\text{out}} = 10^2$ in each run, respectively. Thus, both the parameters n_j and n_{out} satisfy the statistical requirements for the simulations in our study. Since n_{out} is smaller in kMC simulations, we observe larger deviations in $\langle E_{vm} \rangle$ than that of $\langle E_{vf} \rangle$. The simulated bulk material $\text{Me}_{1-x}\text{C}_{1-y}$ has at least 64 vacancies when $x = 0.2\%$, which is much larger than 30 we established as a minimum. From the results of the scaling law, we observe that the mean displacements for both Me and C vacancies show little change during the simulations providing further evidence that our choice of simulation parameters do indeed meet the statistical requirements.

- [1] W. Fahrenholtz, E. Wuchina, W. Lee, and Y. Zhou, *Ultra-High Temperature Ceramics: Materials for Extreme Environment Applications* (Wiley, Hoboken, NJ, 2014).
- [2] T. Y. Kosolapova, The applications of carbides, in *Carbides* (Springer, New York, NY, 1971), pp. 257–263.
- [3] T. Courtney, *Mechanical Behavior of Materials: Second Edition* (Waveland Press, Long Grove, IL, 2005), Chap. 7, pp. 293–353.
- [4] J. L. Chermant, G. Leclerc, and B. L. Mordike, Deformation of titanium carbide at high temperature, *Zeitschrift fuer Metallkunde* **71**, 465 (1980).
- [5] C. Kim, G. Gottstein, and D. Grummon, Plastic flow and dislocation structures in tantalum carbide: Deformation at low and intermediate homologous temperatures, *Acta Metall. Mater.* **42**, 2291 (1994).
- [6] R. Steinitz, *Mechanical Properties of Refractory Carbides at High Temperatures* (American Nuclear Society, La Grange Park, IL, 1966), pp. 75–100.
- [7] C. J. Smith, M. A. Ross, N. D. Leon, C. R. Weinberger, and G. B. Thompson, Ultra-high temperature deformation in TaC and HfC, *J. Eur. Ceram. Soc.* **38**, 5319 (2018).
- [8] X.-X. Yu, G. B. Thompson, and C. R. Weinberger, Influence of carbon vacancy formation on the elastic constants and hardening mechanisms in transition metal carbides, *J. Eur. Ceram. Soc.* **35**, 95 (2015).
- [9] S. Sarian, Diffusion of carbon in TiC, *J. Appl. Phys.* **39**, 3305 (1968).
- [10] V. S. Eremeev and A. S. Panov, Diffusion of carbon in vanadium and titanium carbides, *Powder Metall. Met. Ceram.* **6**, 306 (1967).
- [11] F. J. J. van Loo and G. F. Bastin, On the diffusion of carbon in titanium carbide, *Metall. Trans. A* **20**, 403 (1989).
- [12] S. Sarian, Diffusion of ^{44}Ti in TiC_x , *J. Appl. Phys.* **40**, 3515 (1969).
- [13] W. F. Brizes, Diffusion of carbon in the carbides of tantalum, *J. Nucl. Mater.* **26**, 227 (1968).
- [14] R. Resnick, R. Steinitz, and L. Seigle, Determination of diffusivity of carbon in tantalum and columbium carbides by layer-growth measurements, *Trans. Metall. Soc. AIME* **233**, 1915 (1965).
- [15] R. Resnick and L. Seigle, The diffusion of carbon in tantalum monocarbide, *Trans. Metall. Soc. AIME* **236**, 1732 (1966).
- [16] B. B. Yu and R. F. Davis, Self-diffusion of ^{95}Nb in single crystals of NbC_x , *J. Phys. Chem. Solids* **42**, 83 (1981).
- [17] X.-X. Yu, C. R. Weinberger, and G. B. Thompson, *Ab initio* investigations of the phase stability in group IVB and VB transition metal carbides, *Comput. Mater. Sci.* **112**, 318 (2016).
- [18] E. Gross and R. Dreizler, *Density Functional Theory*, Nato Science Series B (Springer, New York, NY, 2013).
- [19] M. Rålander, H. W. Hugosson, and A. Delin, Density functional study of carbon vacancies in titanium carbide, *J. Phys.: Condens. Matter* **30**, 015702 (2017).
- [20] V. I. Razumovskiy, P. A. Korzhavyi, and A. V. Ruban, *Ab initio* calculations of kinetic properties in ZrC and TiC carbides, in *Solid-Solid Phase Transformations in Inorganic Materials*, Solid State Phenomena, edited by Y. Bréchet, E. Clouet, A. Deschamps, A. Finel, and F. Soisson (Trans Tech Publications Ltd., Stafa-Zurich, Switzerland, 2011), Chap. 9, pp. 990–995.
- [21] V. I. Razumovskiy, A. V. Ruban, J. Odqvist, and P. A. Korzhavyi, Vacancy-cluster mechanism of metal-atom diffusion in substoichiometric carbides, *Phys. Rev. B* **87**, 054203 (2013).
- [22] W. Sun, H. Ehteshami, P. R. Kent, and P. A. Korzhavyi, Self-diffusion of Ti interstitial based point defects and complexes in TiC, *Acta Mater.* **165**, 381 (2019).
- [23] H. Yu, M. Bahadori, G. B. Thompson, and C. R. Weinberger, Understanding dislocation slip in stoichiometric rocksalt transition metal carbides and nitrides, *J. Mater. Sci.* **52**, 6235 (2017).
- [24] N. De Leon, B. Wang, C. R. Weinberger, L. E. Matson, and G. B. Thompson, Elevated-temperature deformation mechanisms in Ta_2C : An experimental study, *Acta Mater.* **61**, 3905 (2013).
- [25] C. R. Weinberger and G. B. Thompson, Review of phase stability in the group IVB and VB transition-metal carbides, *J. Am. Ceram. Soc.* **101**, 4401 (2018).
- [26] A. I. Gusev, Order-disorder transformations and phase equilibria in strongly nonstoichiometric compounds, *Phys. Usp.* **43**, 1 (2000).
- [27] N. Metropolis, A. W. Rosenbluth, M. N. Rosenbluth, A. H. Teller, and E. Teller, Equation of state calculations by fast computing machines, *J. Chem. Phys.* **21**, 1087 (1953).
- [28] W. K. Hastings, Monte Carlo sampling methods using Markov chains and their applications, *Biometrika* **57**, 97 (1970).
- [29] A. F. Voter, Introduction to the kinetic Monte Carlo method, in *Radiation Effects in Solids*, edited by K. E. Sickafus, E. A. Kotomin, and B. P. Uberuaga (Springer, Netherlands, Dordrecht, 2007), pp. 1–23.
- [30] W. Cai, W. Nix, and M. R. Society, *Imperfections in Crystalline Solids*, MRS-Cambridge Materials Fundamentals (Cambridge University Press, Cambridge, 2016), Chap. 7, pp. 175–201.
- [31] P. E. Blöchl, Projector augmented-wave method, *Phys. Rev. B* **50**, 17953 (1994).
- [32] G. Kresse and D. Joubert, From ultrasoft pseudopotentials to the projector augmented-wave method, *Phys. Rev. B* **59**, 1758 (1999).
- [33] J. P. Perdew, J. A. Chevary, S. H. Vosko, K. A. Jackson, M. R. Pederson, D. J. Singh, and C. Fiolhais, Atoms, molecules, solids, and surfaces: Applications of the generalized gradient approximation for exchange and correlation, *Phys. Rev. B* **46**, 6671 (1992).
- [34] J. P. Perdew, K. Burke, and M. Ernzerhof, Generalized Gradient Approximation Made Simple, *Phys. Rev. Lett.* **77**, 3865 (1996).
- [35] C. R. Weinberger and G. B. Thompson, A computational search for the zeta phase in the tantalum carbides, *J. Am. Ceram. Soc.* **102**, 1454 (2019).
- [36] C. R. Weinberger and G. B. Thompson, The crystal structure and phase stability of the zeta phase in the group VB transition metal carbides: A computational investigation, *Acta Crystallogr., Sect. B: Struct. Sci., Cryst. Eng. Mater.* **75**, 870 (2019).
- [37] J. M. Sanchez, The cluster expansion method, in *Theory and Applications of the Cluster Variation and Path Probability Methods*, edited by J. L. Morán-López and J. M. Sanchez (Springer US, Boston, 1996), pp. 175–185.
- [38] J. Sanchez, F. Ducastelle, and D. Gratias, Generalized cluster description of multicomponent systems, *Physica A: Stat. Mech. Appl.* **128**, 334 (1984).
- [39] Q. Wu, B. He, T. Song, J. Gao, and S. Shi, Cluster expansion method and its application in computational materials science, *Comput. Mater. Sci.* **125**, 243 (2016).
- [40] J. M. Sanchez, Foundations and practical implementations of the cluster expansion, *J. Phase Equilib. Diffus.* **38**, 238 (2017).

- [41] J. Stoer, R. Bartels, W. Gautschi, R. Bulirsch, and C. Witzgall, *Introduction to Numerical Analysis*, Texts in Applied Mathematics (Springer, New York, 2002), Chap. 4, pp. 232–243.
- [42] R. L. Wasserstein and N. A. Lazar, The ASA statement on p-values: Context, process, and purpose, *Am. Stat.* **70**, 129 (2016).
- [43] J. Devore, *Probability and Statistics for Engineering and the Sciences* (Cengage Learning, Boston, MA, 2015), Chap. 14, pp. 594–624.
- [44] G. Shieh, Improved shrinkage estimation of squared multiple correlation coefficient and squared cross-validity coefficient, *Org. Res. Meth.* **11**, 387 (2008).
- [45] D. Sholl and J. Steckel, *Density Functional Theory: A Practical Introduction* (Wiley, Hoboken, NJ, 2009), Chap. 6, pp. 131–157.
- [46] B. Yu and R. Davis, Self-diffusion of ^{14}C in single crystals of NbC_x , *J. Phys. Chem. Solids* **40**, 997 (1979).
- [47] G. H. Vineyard, Frequency factors and isotope effects in solid state rate processes, *J. Phys. Chem. Solids* **3**, 121 (1957).
- [48] G. Ho, M. T. Ong, K. J. Caspersen, and E. A. Carter, Energetics and kinetics of vacancy diffusion and aggregation in shocked aluminium via orbital-free density functional theory, *Phys. Chem. Chem. Phys.* **9**, 4951 (2007).
- [49] S. P. Dodd, M. Cankurtaran, and B. James, Ultrasonic determination of the elastic and nonlinear acoustic properties of transition-metal carbide ceramics: Tic and Tac, *J. Mater. Sci.* **38**, 1107 (2003).
- [50] S. Brooks, A. Gelman, G. Jones, and X. L. Meng, *Handbook of Markov Chain Monte Carlo*, Chapman & Hall/CRC Handbooks of Modern Statistical Methods (CRC Press, Boca Raton, FL, 2011).
- [51] A. Einstein, Über die von der molekularkinetischen theorie der wärme geforderte bewegung von in ruhenden flüssigkeiten suspendierten teilchen, *Annalen der Physik* **322**, 549 (1905).
- [52] N. Fricke, J. Zierenberg, M. Marenz, F. P. Spitzner, V. Blavatska, and W. Janke, Scaling laws for random walks in long-range correlated disordered media, *Condens. Matter Phys.* **20**, 13004 (2017).
- [53] J. M. Cowley, Short-range order and long-range order parameters, *Phys. Rev.* **138**, A1384 (1965).
- [54] See Supplemental Material at <http://link.aps.org/supplemental/10.1103/PhysRevMaterials.4.093602> for an example animation of the kMC simulation of in a repetition of the conventional cell (smaller than the simulated systems in this paper): Ti atom-blue sphere; C atom-yellow sphere; Ti vacancy-black sphere; C vacancy-red sphere.
- [55] N. De Leon, X.-X. Yu, H. Yu, C. R. Weinberger, and G. B. Thompson, Bonding Effects on the Slip Differences in the B1 Monocarbides, *Phys. Rev. Lett.* **114**, 165502 (2015).
- [56] J. Ziman, *Electrons and Phonons: The Theory of Transport Phenomena in Solids*, Oxford classic texts in the physical sciences (Clarendon, Oxford, 1960).
- [57] N. Ashcroft, M. Ashcroft, D. Wei, N. Mermin, and C. Learning, *Solid State Physics: Revised Edition* (Cengage Learning Asia, Boston, MA, 2016), Chap. 14, pp. 263–282.
- [58] F. Zhou, T. Maxisch, and G. Ceder, Configurational Electronic Entropy and the Phase Diagram of Mixed-Valence Oxides: The Case of Li_xFePO_4 , *Phys. Rev. Lett.* **97**, 155704 (2006).
- [59] V. Ern and A. C. Switendick, Electronic band structure of TiC, TiN, and TiO, *Phys. Rev.* **137**, A1927 (1965).
- [60] V. Zhukov and V. Gubanov, The study of the energy band structures of TiC, VC, Ti_4C_3 and V_4C_3 by the LMTO-ASA method, *J. Phys. Chem. Solids* **48**, 187 (1987).
- [61] M. Sahnoun, C. Daul, J. Parlebas, C. Demangeat, and M. Driz, Electronic structure and optical properties of TaC from the first principles calculation, *Eur. Phys. J. B* **44**, 281 (2005).
- [62] S. Baroni, S. de Gironcoli, A. Dal Corso, and P. Giannozzi, Phonons and related crystal properties from density-functional perturbation theory, *Rev. Mod. Phys.* **73**, 515 (2001).
- [63] E. I. Isaev, S. I. Simak, I. A. Abrikosov, R. Ahuja, Y. K. Vekilov, M. I. Katsnelson, A. I. Lichtenstein, and B. Johansson, Phonon related properties of transition metals, their carbides, and nitrides: A first-principles study, *J. Appl. Phys.* **101**, 123519 (2007).
- [64] R. G. Lye and E. M. Logothetis, Optical properties and band structure of titanium carbide, *Phys. Rev.* **147**, 622 (1966).
- [65] A. L. Drago, Diffusion rates in inorganic nuclear materials, *J. Res. Natl. Bur. Stand., Sect. A* **72A**, 157 (1968).
- [66] R. Hogg, J. McKean, and A. Craig, *Introduction to Mathematical Statistics*, Pearson education international (Pearson Education, New York, NY, 2005), Chap. 4, pp. 122–180.
- [67] W. Feller, *An Introduction to Probability Theory and its Applications*, Wiley Series in Probability and Mathematical Statistics. Probability and Mathematical Statistics No. v. 2 (Wiley, Hoboken, NJ, 1966), Chap. 6, pp. 146–169.
- [68] G. Box, W. Hunter, and J. Hunter, *Statistics for Experimenters: An Introduction to Design, Data Analysis, and Model Building*, Wiley Series in Probability and Mathematical Statistics: Applied Probability and Statistics (Wiley, Hoboken, NJ, 1978), Chap. 5, pp. 107–151.
- [69] H. Lancaster, *The Chi-Squared Distribution*, Wiley Series in Probability and Mathematical Statistics. Probability and Mathematical Statistics (Wiley, Hoboken, NJ, 1969).